Master Thesis

Thin Layer Optics in Photomultipliers: A Geant4 Simulation and Comparison to Ellipsometric Measurements

Supervisor:
Prof. Dr. Alexander Kappes

Second examiner:
Apl. Prof. Dr. Alfons Khoukaz

A thesis submitted in fulfillment of the requirements for the degree of

Master of Science *at* University Münster

by

Nicolai Krybus

AG Kappes
Institute of Nuclear Physics

8 August 2024

Declaration of Academic Integrity

I hereby confirm that this thesis on "Thin Layer Optics in Photomultipliers: A Geant4 Simulation and Comparison to Ellipsometric Measurements" is solely my own work and that I have used no sources or aids other than the ones stated. All passages in my thesis for which other sources, including electronic media, have been used, be it direct quotes or content references, have been acknowledged as such and the sources cited.

Münster, 8 August 2024 _____

I agree to have my thesis checked in order to rule out potential similarities with other works and to have my thesis stored in a database for this purpose.

Münster, 8 August 2024 _____

"*Estragon: Und wenn er kommt? / Wladimir: Sind wir gerettet.*"

- Samuel Beckett, Warten auf Godot

Contents

1 Introduction

There are many ways to look into the night's sky. One could just tilt their head up and catch electromagnetic waves between around 400 nm to 700 nm wavelengths with their eyes. One could also use a radio telescope to catch electromagnetic waves with wavelengths between 3 mm an 30 m and will find a completely different view. Of course it does not stop there: by now people all around the Earth are looking for many different messengers of events deep in the universe. From visible light, to gamma rays and cosmic rays, to gravitational waves or neutrinos. Humans have developed remarkable creativity in their quest to learn more about the universe.

The key word is "multi-messenger astronomy": each of the previously mentioned messengers has its own advantages and disadvantages hence physicists study events through multiple different lenses. Electromagnetic waves for example point directly towards their sources since they do not carry mass, but on the other hand they are easily absorbed by star dust or other objects in their path. In addition, similar gamma rays are generated in very different processes which can lead to confusion. Cosmic rays offer valuable, high-energy information that is essential for multi-messenger astronomy. Their ability to travel vast distances, often preserving information about their origin, provides unique insights into high-energy processes and extreme conditions. However, their trajectories are deflected by magnetic fields in the universe, making it challenging to trace them back to their sources, which remains one of the major mysteries in science today. Moreover, upon entering the Earth's atmosphere, cosmic rays create secondary particles, often leading to entire particle showers, complicating the analysis of the original events.

Similarly to gamma rays, neutrinos also point directly towards their sources due to their very small mass, but unlike gamma rays, neutrinos interact very rarely and are therefore very likely to reach us untouched. This is a very important feature, since it conserves valuable information about the origin of said particle, but it is also the greatest difficulty in detecting neutrinos, since they interact on Earth just as rarely as on their way towards it. That is why the **IceCube Collaboration** [1] designed a large scale neutrino telescope - the **IceCube Neutrino Observatory** - at the South Pole consisting of over 5000 optical modules inside the deep ice to form a $1\,\mathrm{km}^3$ detection volume. Here it is currently possible to detect signatures from neutrinos in a range from around 6 GeV to high PeV energies. This leads to **IceCube Upgrade**, where a new generation of optical modules and calibration devices will be implemented to further improve the measurement of low energy neutrinos down to 1 GeV, neutrino oscillation, tau-neutrinos and the understanding of Cherenkov light propagation produced by neutrino interactions inside the ice [1]. One of these new optical modules is the **mDOM**, which features 24 photomultiplier tubes (PMTs) that are capable of detecting even single photons produced by cosmic neutrinos [2]. This is possible due to high precision calibration of the detection process of every single photon that reaches a PMT .

This thesis further investigates optical phenomena on thin layers in the outer shell of a

PMT that have an impact on the detection efficiency of each sensor and therefore play a crucial part in the detection process in IceCube Upgrade. This is to be be achieved by creating a **GEANT4** simulation framework for the optical system that is made of the glass shell of a PMT together with the photocathode layer. The results are then to be compared to reflectance and transmittance measurements on simplified samples to validate the results.

In Chapter 2, the basics of neutrino properties and their detection using the IceCube Neutrino Observatory are discussed, along with an explanation of photomultiplier tubes. Chapter 3 provides the theoretical groundwork for understanding light propagation at interfaces between media and includes a detailed analysis of optical phenomena in thin layers. Chapter 4 introduces the *Geant4* framework, detailing its setup for simulating light propagation in media and the necessary implementations for this work. Chapter 5 describes the measurement setup and the samples used to verify the previous calculations and simulations. The analysis of these measurements, along with comparisons between theory, simulation, and experiment, is presented in Chapter 6. Finally, Chapter 7 summarizes the key results, assesses their implications, and discusses future applications of these findings for PMTs at IceCube.

2 Neutrino Astronomy

In the following chapter we take a deeper look into the fundamental properties of neutrinos, why they are interesting for astronomy and the basic detection principle of the IceCube Neutrino Observatory.

2.1 Neutrinos in the Standard Model

Neutrinos are fundamental particles of the Standard Model of particle physics. The Standard Model postulates 17 particles that are shown in Figure 2.1. These particles are classified into fermions and bosons, the fermions comprising the quarks and the leptons and where the bosons consist of the four gauge bosons and the Higgs boson. Fermions are the building blocks of matter, with quarks combining to form protons and neutrons, and the electron, a lepton, orbiting around the nucleus of atoms. Bosons are force carriers: photons mediate the electromagnetic force, gluons are responsible for the strong nuclear force, W and Z bosons govern the weak nuclear force, and the Higgs boson gives particles their mass through the Higgs mechanism [3, 4].

To each fermion there also exists an antiparticle of equal mass, but with the opposite electric charge. Together, these particles and forces describe the fundamental interactions

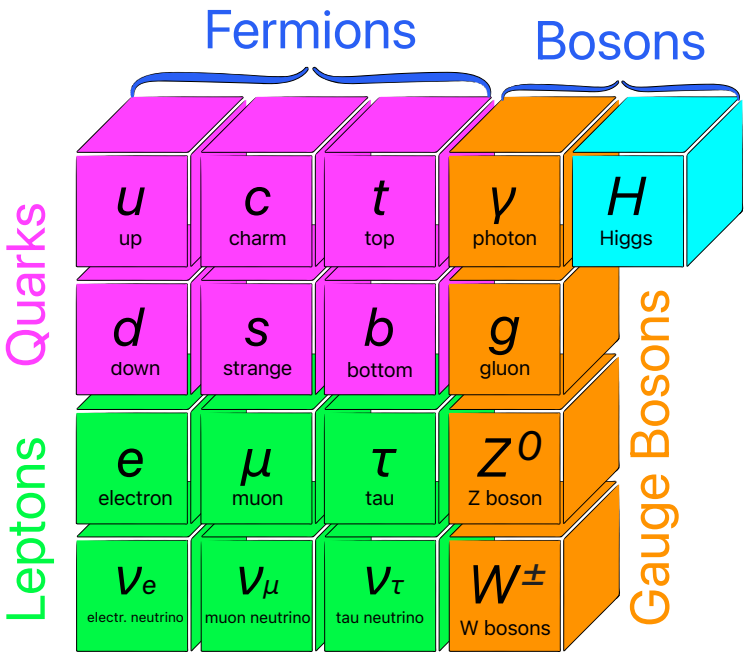

Figure 2.1: Elementary particles of the Standard Model of particle physics. Shown are the 17 fundamental particles grouped into quarks, leptons, gauge bosons and the Higgs boson based on [3].

that govern the behavior of matter in the universe. Neutrinos, a type of lepton, are particularly intriguing within the Standard Model due to their unique properties. Unlike other particles, neutrinos are extremely light, electromagnetically neutral and only interact via the weak nuclear force and gravity, making them exceptionally elusive. There are three types, or flavors, of neutrinos: electron neutrinos, muon neutrinos, and tau neutrinos, each associated with their corresponding charged leptons [3, 5, 4].

Neutrinos rarely interact with matter, allowing them to travel vast distances through space virtually undisturbed, which makes them valuable messengers in astronomy [6]. However, their small interaction cross section also poses significant challenges for detection: it is near impossible to detect neutrinos directly. Instead, researchers rely on indirect detection methods by observing secondary particles produced from neutrino interactions with matter. This necessitates sophisticated and large-scale observatories like the IceCube Neutrino Observatory [5]. The following section will further explain the intricacies of neutrino interactions.

2.2 Neutrino Interactions

Neutrinos are certainly not rare particles. On Earth, tens of billions of neutrinos pass through an area of the size of a human thumbnail every second [7]. These can, for example, stem from processes in the sun (solar neutrinos), or from particle showers caused by cosmic particles (atmospheric neutrinos) that have reached the Earth. These come with energies in the eV- to MeV range [8]. However, while these lower-energy neutrinos provide valuable information about their sources, it is the high-energy neutrinos (several hundred GeV and more) that are of special interest to researchers of the extragalactic universe. High-energy neutrinos, which are produced in some of the most energetic and extreme environments in the universe such as supernovae, active galactic nuclei, and gamma-ray bursts, offer unique insights into these powerful cosmic phenomena. Their detection and study are crucial for advancing our understanding of the universe's most violent and energetic processes.

As previously mentioned neutrinos are neutral and therefore not affected by magnetic fields on their path towards Earth. Due to their very small cross section they might surpass entire galaxies without interacting once [5]. This means that a neutrino reaching Earth likely still retains its original trajectory and energy from when it was originally produced - a huge advantage for astronomical observations compared to charged particles or even photons. Another useful feature of high-energy neutrinos is the fact, that they are a so called "smoking gun" for hadronic interactions. This characteristic can make it easier to trace them back to their astrophysical sources compared to gammas, which can be produced in both hadronic and leptonic interactions, thereby complicating source identification. But all of these points combined also make it extremely complicated to detect cosmic neutrinos in the first place since the same cross section of course still applies on Earth while also the abundance of high-energy neutrinos is magnitudes lower than for example solar or atmospheric neutrinos. This is why the search for cosmic neutrinos is near impossible without large scale detection volumes like at the IceCube Neutrino Observatory [4, 5].

With the current state-of-the-art measurement techniques, direct detection of neutrinos remains impossible. Instead, scientists detect charged secondary particles produced by weak interactions. The weak force is mediated by the Z^0, W^+, and W^- bosons. Interactions involving the neutral Z^0 boson are referred to as neutral current (NC) interactions, while those involving the charged $W^\pm$ bosons are known as charged current (CC) interactions. For high-energy neutrinos in the range of GeV to several PeV the relevant cause of interaction is the deep inelastic scattering at a nucleus. These interactions can be represented as follows:

$$\text{CC: } \overset{(-)}{\nu}_\ell + \text{N} \xrightarrow{W^\pm} \ell^\mp + \text{X}, \quad \text{NC: } \overset{(-)}{\nu}_\ell + \text{N} \xrightarrow{Z^0} \overset{(-)}{\nu}_\ell + \text{X}, \tag{2.1}$$

where $\overset{(-)}{\nu}_\ell$ is a (anti-)neutrino of flavor ℓ and N is a nucleon, i.e. either a proton or a neutron. In the case of CC-interactions, this results in a $\ell^\mp$ of the neutrinos flavor, together with X, which can be either several new hadronic particles or even an entire cascade of those. In contrast, in NC-processes there is an outgoing neutrino of the same flavor accompanied again by a hadronic particle. If the resulting particles carry charge it is possible for them to cause Cherenkov radiation in a suitable detector, which will be explained in the following part [4, 6].

2.3 Cherenkov radiation and detection principle

Understanding the generation of Cherenkov light, or Cherenkov radiation, is essential to understand the functioning of the IceCube Neutrino Observatory. This phenomenon is the primary method used for the indirect detection of neutrinos. Cherenkov radiation occurs when a charged particle, such as an electron or muon, travels through a dielectric medium, like water or ice, at a velocity v greater than the phase velocity of light $c_n = c/n$ in said medium, where n is the refractive index of the medium and c is the speed of light. This results in the emission of a cone of light along the particle's path. The effect is analogous to the sonic boom produced by an object moving faster than the speed of sound in air. The radiation is generated through a rather complex process, where the fast moving charged particle induces temporary dipoles in the medium [4].

Since the charged particle moves faster than the speed of light in the medium, the polarization is not able to keep up with the induction of new dipoles and the radiation interferes constructively, as can be seen in Figure 2.2. The opening angle of the cone is characteristic for a particle at certain speed v in a medium of refractive index n and be calculated using the relation

$$\theta_C = \arccos\left(\frac{c}{n \cdot v}\right), \tag{2.2}$$

which results in a characteristic angle of around 40° in ice with $n_{\text{ice}} \approx 1.3$ [10].

The intensity of the radiation is very low and hard to detect. Therefore it is necessary to be highly sensitive to the wavelength of this radiation and also transparent enough for the wave to reach a sensor to observe these elusive signals (which is why the medium is ice in this case). Detecting Cherenkov radiation from high-energy neutrinos requires

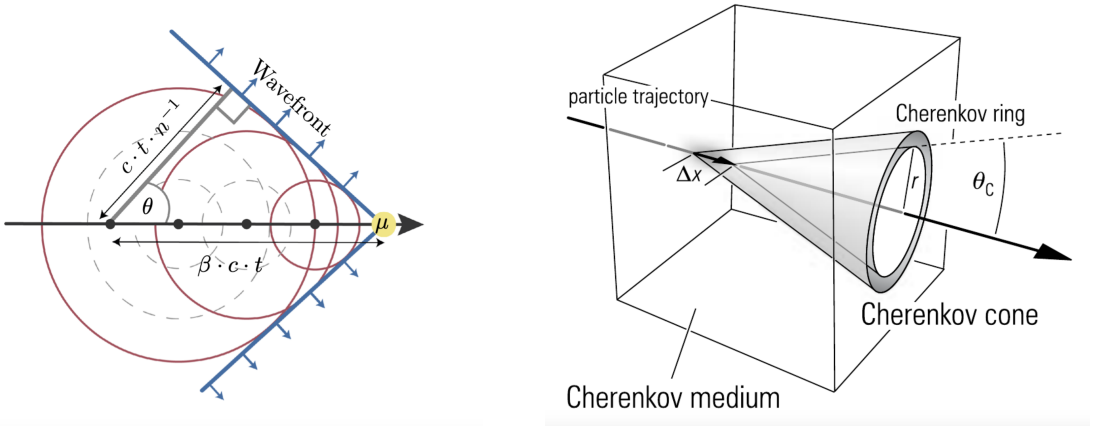

Figure 2.2: Left: Sketch of a Cherenkov cone emitted by a muon traversing through a medium with refractive index n. The circular waves form a straight wave front at the characteristic Cherenkov angle θ. Figure taken from [9]. Right: Sketch of a Cherenkov cone around a particles trajectory inside a volume. Taken from [8 (p. 56)].

a vast detection volume and an array of sophisticated sensors to capture the faint light produced by these interactions [4]. An experiment of this magnitude necessitates extensive planning and collaboration among scientists from around the globe, a collective effort that culminated in the IceCube collaboration.

2.4 The IceCube Neutrino Observatory

Located at the Amundsen-Scott South Pole Station near the geographic south pole (see Figure 2.3) lies the heart of the IceCube observatory: the 1 km^3 instrumented volume deep inside the glacial ice that make it currently the largest neutrino detector on Earth. Below the Amundsen-Scott South Pole Station the detector lies at a depth of between around 1.5 km and 2.5 km. It consists of 5160 digital optical modules (DOMs) that are attached to 86 strings that have been let into the ice at a distance of around 125 m to each other. Each of the modules is equipped with a 24 cm photomultiplier tube (PMT) that is able to detect the Cherenkov radiation produced by charged particles. Around the center of the detection volume eight additional strings form the **DeepCore** region which is optimized to detect neutrinos of even lower energies down to 6 GeV [1]. At the surface around the pole station lies **IceTop**, a cosmic air shower array made out of ice filled tanks equipped with DOMs, that detects air showers and can act as a veto for atmospheric muons [11]. Figure 2.4 shows a schematic illustration of the whole detector.

Figure 2.3: Picture of the Amundsen-Scott South Pole Station. Courtesy of the IceCube Collaboration.

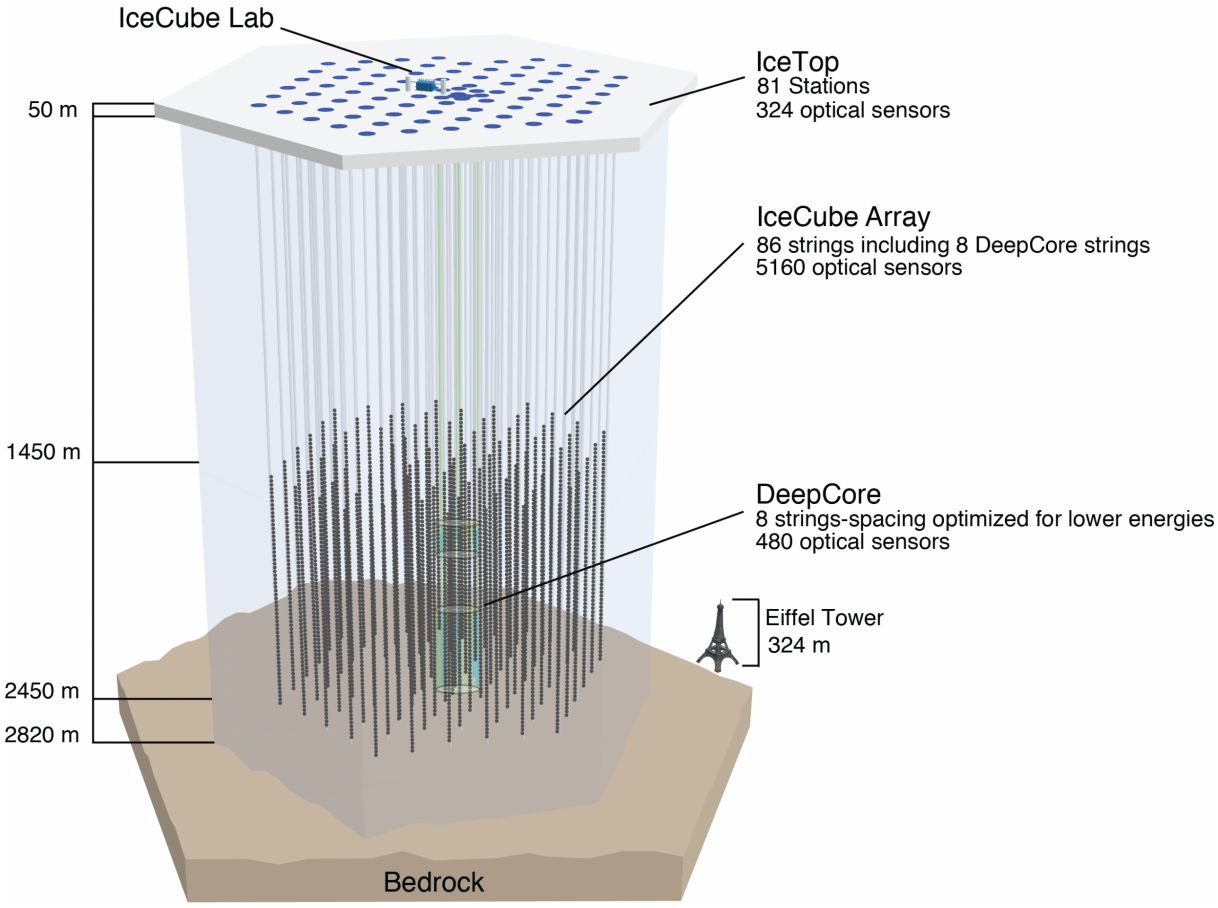

Figure 2.4: Sketch depicting the IceCube Neutrino Observatory consisting of surface and in-ice components, including IceTop, the IceCube In-Ice Array, and DeepCore. Figure courtesy of the IceCube collaboration.

The IceCube Neutrino Observatory is designed to detect neutrinos with energies ranging from 100 GeV (excluding DeepCore) to several PeV. By analyzing the accumulated photons detected by the photomultiplier tubes (PMTs) within the detection volume, it is possible to estimate the energy deposited by a particle inside the detector and, consequently, infer the particle's energy, given that the event is fully contained in the detection volume. The PMTs also provide precise timing information, which allows for the reconstruction of the particle's trajectory and the determination of its direction of origin. The distinct signal patterns, which can range from diffuse spheres called **cascades** to straight **tracks** (see Figure 2.5). Both NC- and CC-interactions cause hadronic showers, that appear as spherical signatures in the array of optical modules. In CC-interactions including ν_e ($\bar{\nu}_e$) an electron (positron) will be emitted. These cause an electromagnetic shower that only has a range of a few meters, which makes it impossible to separate from the initial hadronic shower. Since these spheres are small, they can be completely contained inside the detection volume what makes it possible to infer the total energy deposited by the initial neutrino. For ν_μ ($\bar{\nu}_\mu$) on the other hand, the CC-interactions result in a muon, that can travel long distances inside the ice, where they leave behind a track of activated modules. This track allows for very precise directional reconstruction, but the initial muon energy can only be deduced if the track is entirely contained inside the detection volume, which is not necessarily the case. A track also allows the identification

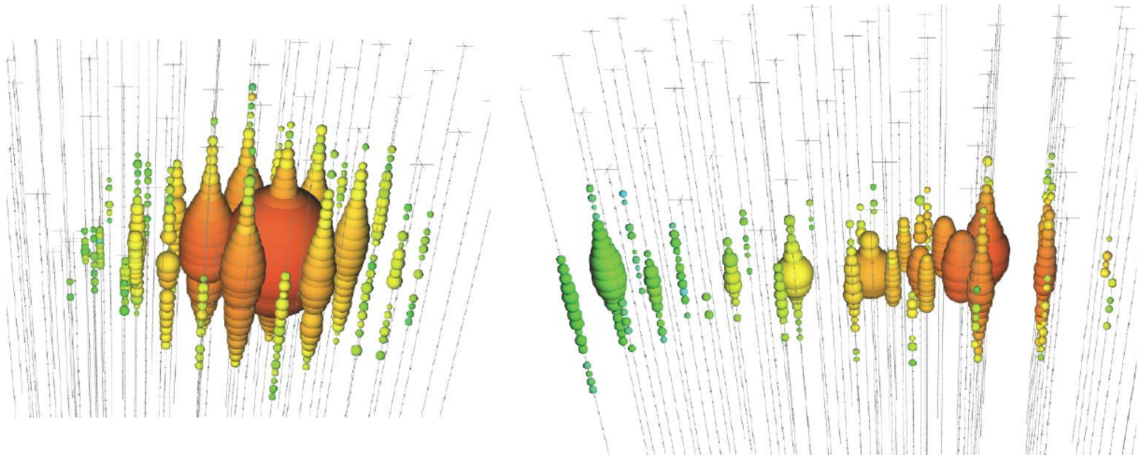

Figure 2.5: Examples of two simulated events with different signatures. Each bubble is a DOM that detected a signal. Larger bubbles are proportional to more detected light, the color corresponds to the relative time of detection (red: first, green: later). The left event shows a cascade, while the right one is more track-like and belongs to an muon (anti-)neutrino. Picture courtesy of the IceCube collaboration.

of a ν_μ ($\bar{\nu}_\mu$). Lastly, taus emitted from CC-interactions involving ν_τ ($\bar{\nu}_\tau$) have a very short lifetime, after which they decay most likely into a neutrino together with a lighter lepton or meson, where the latter two will produce a cascade very similar to an initial ν_e which makes them hard to distinguish. Only if the ν_τ has a very high energy of several hundred TeV one is able to visually identify it as a **double bang**, that would look like two spherical signatures behind each other [12, 5].

2.5 IceCube Upgrade and Gen2

The next two steps for expanding the capabilities of the IceCube Neutrino Observatory are **IceCube Upgrade** and **IceCube-Gen2**. IceCube Upgrade consists of seven ad-

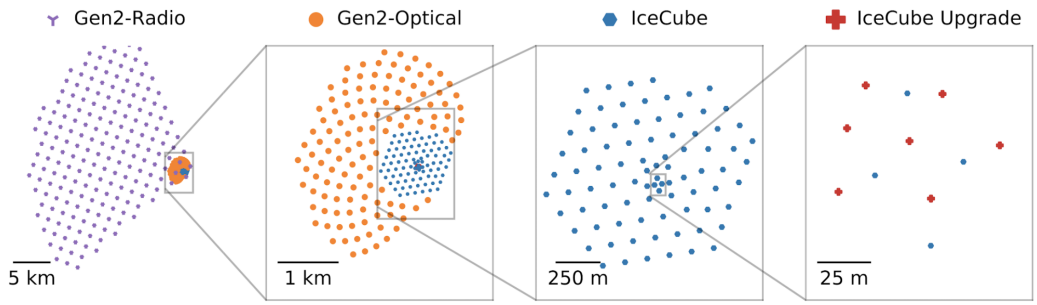

Figure 2.6: Illustration of the integration of planned extensions of IceCube, including IceCube Upgrade and IceCube-Gen2. Figure taken from [13]

ditional strings with 750 advanced photodetectors and calibration devices. These are used to enhance the measurement of low energy neutrinos, by lowering the sensitivity threshold to around 1 GeV, improving the understanding of light propagation inside the

ice, enabling the detection of tau neutrinos and facilitating neutrino oscillation analyses among other high precision measurements. IceCube-Gen2 plans to increase to detection volume inside the ice by a factor of eight approximately with a radio array on top. Figure 2.6 shows an illustration of how these expansions place into the current IceCube setup. Among other new sensors, IceCube Upgrade will deploy the "multi PMT optical module", or short mDOM. These feature 24 80 mm PMTs produced by *Hamamatsu Photonics* arranged all around the module (instead just one, large PMT facing a single direction used in the DOMs at IceCube before). A photograph of an mDOM is shown in Figure 2.7.

Figure 2.7: Picture of an mDOM. The yellow-tinted components are the 24 PMTs.

The mDOM is part of several improvements to the sensitivity of IceCube. One notable enhancement is the ability to obtain directional information from a single module. It is of utmost importance to understand the inner workings of the mDOMs to accurately interpret the scientific data they produce. A thorough understanding of the PMTs used is essential for ensuring the reliability and accuracy of the detected signals, as even small deviations can significantly impact results. This thesis will examine thin layer-optical effects at the surface of the installed PMTs, which are detailed in the following chapters.

2.6 Photomultiplier Tubes

Photomultiplier tubes are a common way for scientists to detect electromagnetic radiation at very low intensities, down to single photons. Their practicality and cost efficiency per effective area make them suitable for large-scale projects like this one. The PMTs used in the mDOM are shaped like light bulbs and consist of an evacuated glass shell with a photocathode layer on the inside and a dynode system in the lower part that attracts electrons and amplifies them to a measurable signal. Figure 2.8 shows an illustration of the most important parts of a PMT.

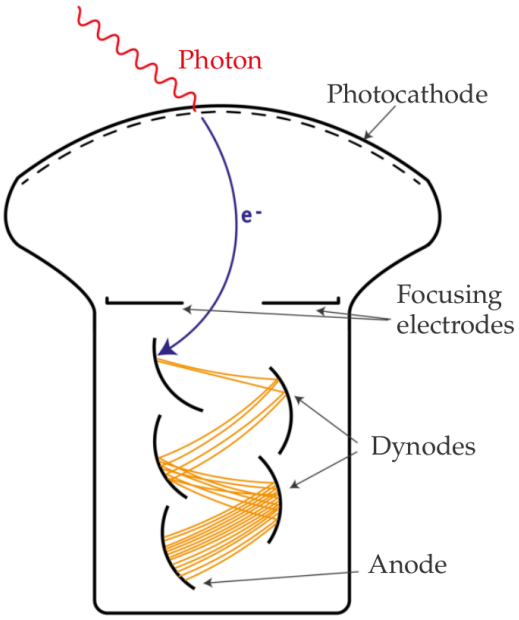

Figure 2.8: Schematic drawing of a PMT and the detection process of a photon that gets converted at the photocathode, attracted towards the first dynode and subsequently multiplied until it reaches the anode as a measurable signal. Figure taken from [14].

When a photon reaches a PMT, it first encounters the borosilicate glass shell. If the photon is not reflected back or absorbed in the glass (optical phenomena such as the likelihood of reflection, transmission, or absorption will be discussed later in chapter 3), it transmits towards the photocathode layer. The **photocathode**,

typically made from a standard bialkali material such as the blue-sensitive Potassium Cesium Antimonide (KCsSb), is applied to the inside of the glass. Potassium Cesium Antimonide is commonly used for photocathodes inside PMTs which are intended to be most sensitive between 400 nm and 500 nm [15], although the exact composition is held a trade mark secret by the manufacturer. When the photon reaches the photocathode layer, it may be reflected or transmitted, but if it is absorbed, a photoelectron may be generated. This process depends on the quantum efficiency (QE) of the photocathode, which quantifies the number of photoelectrons emitted N_e per absorbed photon N_γ and can be calculated using

$$\mathrm{QE}(\lambda) = \frac{N_e}{N_\gamma} \tag{2.3}$$

and lies for PMTs of this manufacturer around the order of $\pm 30\%$ at the previously mentioned range of wavelengths [15].

Photoelectrons emitted from the photocathode are guided towards the first dynode by an electric field generated by focusing electrodes and the dynodes. Dynodes are electrodes that emit multiple electrons when struck by an initial electron. The electric potential increases with each successive dynode, causing each newly emitted electron to be drawn towards the next dynode. This process creates a cascade effect, resulting in a multiplication of electrons, which in turn result in a measurable charge. A very important quantity is the so called **gain** of the PMT: the gain represents the amplification factor, indicating how much charge or current can be expected from a single photon that generates a photoelectron. Since the signal amplitude is directly proportional to the intensity of the incident light, this gain allows for the "counting" of incident photons that hit the PMT.

3 Thin Layer Optics

The behavior of light in our everyday life is one of the most accessible examples of physics in action — quite literally seen with our own eyes. A child observes the bending of light in a glass of water, and our eyes function through an impressive degree of optical precision. To fully understand the quantum efficiency of a photomultiplier tube (PMT), it is essential to comprehend how light behaves with the various steps from the first contact of the PMT's glass shell to its detection at the photocathode. As previously mentioned, not every photon that reaches the glass shell of the PMT will be absorbed and counted. Quantifying this probability requires an understanding of how light behaves within different media and at their interfaces. The following summary of optical laws, such as Snell's law and the Fresnel coefficients, is based on the detailed explanations in [16].

Understanding the dual nature of light, which can be described both as particles and electromagnetic waves, is crucial for understanding how light propagates through different media. For most of the following explanations, light will be treated as a wave.

3.1 Polarization

As an electromagnetic wave, light consists of an electric field $\vec{E}$ and a magnetic induction $\vec{B}$, both of which are perpendicular to each other. A key aspect of describing the wave is the orientation of the electric field. This orientation is most easily described using two complex amplitudes, oriented perpendicular to the direction of propagation. In the following the convention where the propagation direction is along the z-axis, with the complex amplitudes denoted as $\vec{E_x}$ and $\vec{E_y}$, is used. Figure 3.1 provides a visualization of these concepts.

From this perspective an electromagnetic wave can be described in the following way:

$$\begin{aligned} \vec{E}(z,t) &= \vec{E}_x(z,t) + \vec{E}_y(z,t) && (3.1)\\ &= \{E_{x,0} \cdot \exp\left[i(\omega t - Kz + \delta_x)\right]\} \cdot \vec{x} + \{E_{y,0} \cdot \exp\left[i(\omega t - Kz + \delta_y)\right]\} \cdot \vec{y} && (3.2) \end{aligned}$$

with the complex amplitudes $E_{x,0}$ and $E_{y,0}$, the angular frequency ω and the propagation number K. The **phase difference** δ, which is the difference between the phases in the x- and y-directions (δ_x and δ_y), determines the polarization state of the wave, which is the superposition of two partial waves. The **intensity** of the wave is given by $I = |E_{z,t}|^2$. If the phase difference is an integer multiple of π (including 0), the wave is considered linearly polarized, and the electric field vector is aligned in only one direction. In Figure 3.1 (a), this is the case where $E_{x,0} = E_{y,0}$, resulting in the electric field being perfectly diagonal at 45°. If the phase difference is $\pi/2$, the field vector starts to rotate in the xy-plane. For positive phase differences the wave is considered right-circular polarized and for negative phase differences left-circular, due to the direction of rotation of the electric field vector. If also $E_{x,0} = E_{y,0}$ the wave is called circularly polarized, as shown in Figure 3.1 (b). This occurs because the wave oscillating along the y-axis advances forward by

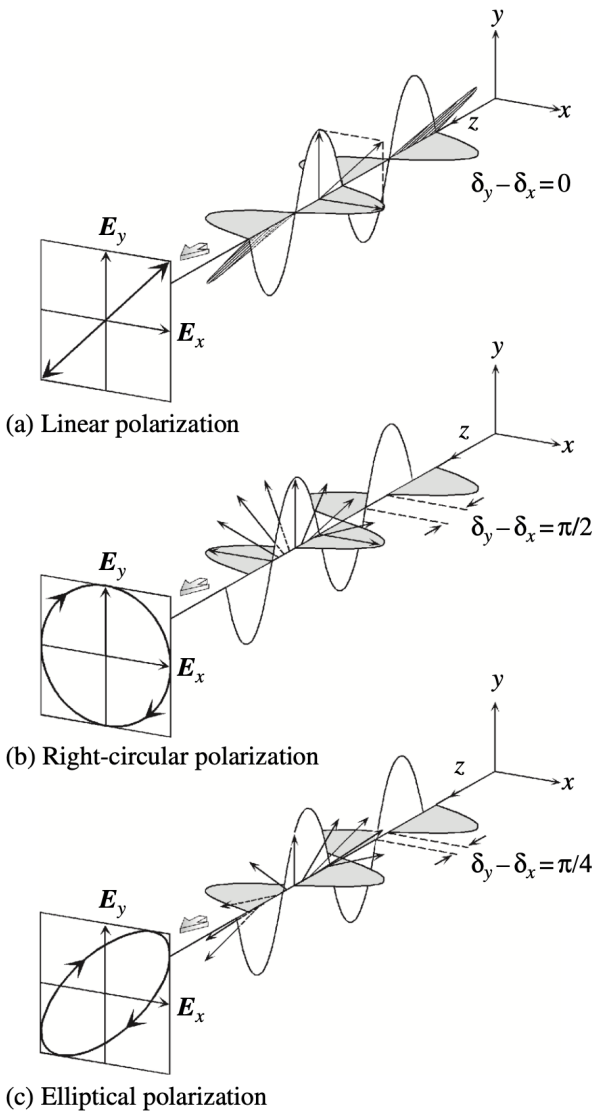

Figure 3.1: Different possible polarization states. The phase differences δ between x- and y-direction and the ratio of E_x and E_y make for different shapes in the x-y-plane. Figure taken from [16].

$\pi/2$ compared to the wave oscillating along the x-axis. For any other case the field vector is considered elliptically polarized, as depicted in Figure 3.1 (c) for a phase difference of $\pi/4$ and also $E_{x,0} = E_{y,0}$.

3.2 Reflection and Transmission at Interfaces

When light propagates within a homogeneous medium, it travels in a straight line. However, its direction changes when it strikes the interface of another medium at an oblique angle. At this point, two partial waves are created: one is reflected back into the incident medium, while the other transmits into the next medium. This phenomenon arises from the varying speed of light in different media. The speed of light in a medium is slower than in a vacuum, according to the relation $c_n = c/n$, where c_n is the speed of light in

the medium and n is the real part of the **refractive index**. The refractive index is a complex property that depends on the wavelength of light. While it is difficult to predict theoretically, it can be determined experimentally through measurements. The complex refractive index is denoted as

$$N = n + ik, \tag{3.3}$$

where n, the real part, primarily determines the refraction of light, and k, the **extinction coefficient**, determines the **absorption length** within the medium[1]. Both n and k depend on the wavelength λ. The extinction coefficient can be related to the absorption length α by

$$\alpha(\lambda) = \frac{\lambda}{4\pi k(\lambda)}. \tag{3.4}$$

For completely transparent media, the extinction coefficient must be close to zero, resulting in a very large absorption length.

Upon striking the interface the direction of the reflected part of the wave is quickly determined by the well-known **law of reflection** "angle of incidence equals angle of reflection", or simply $\theta_i = \theta_r$ as can be seen in Figure 3.2.
Figure 3.2 also visualizes the way the angle of the transmitted wave changes. From considering the lengths of the triangles at different points in the sketch (a detailed derivation is provided in [16]) one can derive **Snell's law**:

$$N_i \sin(\theta_i) = N_t \sin(\theta_t). \tag{3.5}$$

Most of the time, one will encounter this equation with the real part of the refractive index. This might suffice for everyday applications, as long as they use transparent media like air or glass, but as for non-transparent, light absorbing materials it is crucial to include the imaginary part, as will be demonstrated later. When using the complex refractive index, the angles θ_i and θ_t become complex numbers. This concept is not easily visualized, as there is no direct real-world equivalent to imagining a complex angle.

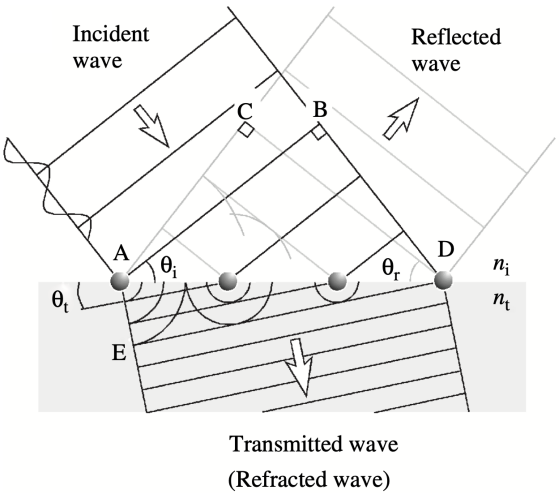

Figure 3.2: Illustration of light reflection and transmission at an oblique incident for $n_i < n_t$. Figure taken from [16].

3.3 Fresnel Equations

As was already introduced, electromagnetic waves feature different polarization or combinations thereof. The orientation of the electric field vector plays a pivotal role when waves

[1]It is important to note that in some literature, including [16], the refractive index is defined as $N = n - ik$. This difference can affect subsequent formulae, so it is crucial to be aware of the author's definition.

strike an interface at oblique incidence. Figure 3.3 visualizes a few important concepts: the electric field components of the incident and reflected waves can both be parameterized in a plane of incidence that is orthogonal to the interface. If the electric field vector lies parallel within this plane, the wave is called **p-polarized**. Conversely, if the electric field is perpendicular to the plane of incidence, the wave is called **s-polarized** (from the German word "senkrecht," meaning perpendicular). In some literature, these are also referred to as "transverse electric" (TE) and "transverse magnetic" (TM) waves, indicating that the respective field is entirely transverse to the direction of propagation, with no component in the propagation direction. Applying this terminology, TE waves correspond to s-polarized light, and TM waves correspond to p-polarized light.

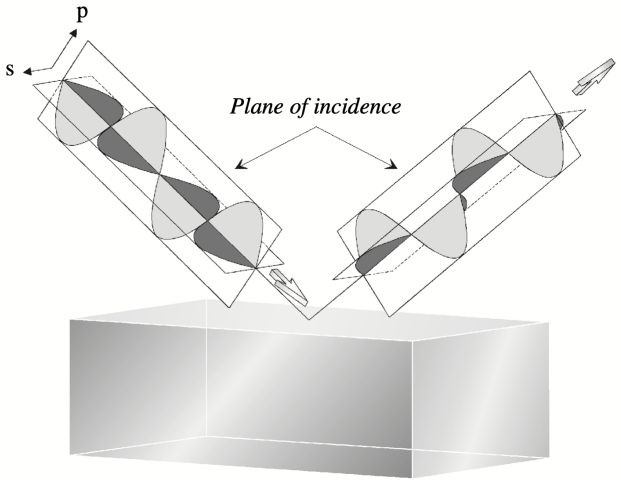

Figure 3.3: Reflection of electromagnetic waves at oblique incident. The p-polarized wave is parallel to the plane of incident, the s-polarized wave is perpendicular. Figure taken from [16].

Upon striking the interface, certain boundary conditions must be met, that are visualized in Figure 3.4. These demand that the components of the electric- ($\vec{E}$) or magnetic ($\vec{B}$) fields that are parallel to the interface (E for p-polarization and the B for s-polarization) are conserved. This results in two equations for each the p-polarized wave

$$E_{ip}\cos(\theta_i) - E_{rp}\cos(\theta_r) = E_{tp}\cos(\theta_t), \tag{3.6}$$

$$B_{ip} + B_{rp} = B_{tp}, \tag{3.7}$$

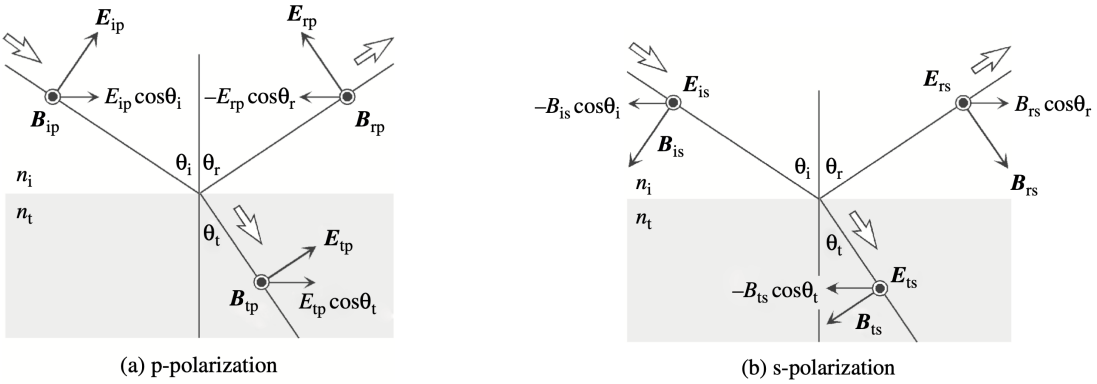

Figure 3.4: Electric field $\vec{E}$ and magnetic field $\vec{B}$ before and after striking the interface between two media for p- **(a)** and s-polarization **(b)**. In **(a)**, $\vec{B}$ is pointing towards the reader, where it is $\vec{E}$ in **(b)**. Figure taken from [16].

as well as for the s-polarized wave:

$$B_{rs}\cos(\theta_r) - B_{is}\cos(\theta_i) = -B_{ts}\cos(\theta_t), \tag{3.8}$$

$$E_{is} + E_{rs} = E_{ts}. \tag{3.9}$$

One can now use the relation $E = c/N \cdot B$ to transform the B-components to the corresponding E-parts. Exemplary for equation 3.7, this transformation would be

$$B_{ip} + B_{rp} = B_{tp} \quad \Rightarrow \quad N_i(E_{ip} + E_{rp}) = N_t E_{tp}. \tag{3.10}$$

From here one can derive the amplitude reflection and transmission coefficients for the wave, which are also known as **Fresnel coefficients**:

$$r_s = \frac{E_{rs}}{E_{is}} = \frac{N_i\cos\theta_i - N_t\cos\theta_t}{N_i\cos\theta_i + N_t\cos\theta_t}, \qquad r_p = \frac{E_{rp}}{E_{ip}} = \frac{N_t\cos\theta_i - N_i\cos\theta_t}{N_t\cos\theta_i + N_i\cos\theta_t}, \tag{3.11}$$

$$t_s = \frac{E_{ts}}{E_{is}} = \frac{2N_i\cos\theta_i}{N_i\cos\theta_i + N_t\cos\theta_t}, \qquad t_p = \frac{E_{tp}}{E_{ip}} = \frac{2N_i\cos\theta_i}{N_t\cos\theta_i + N_i\cos\theta_t}. \tag{3.12}$$

These coefficients indicate the proportion of the incident light's electric field amplitude that is reflected and transmitted at the boundary and are not to be confused with a probability of reflection or transmission. The values are generally complex, can become negative and their absolute can be larger than one. For these coefficients the following relations hold:

$$r_{ij} = -r_{ji} \quad \text{and} \quad t_{ij}t_{ji} = 1 - r_{ij}^2. \tag{3.13}$$

It is possible nevertheless to calculate the **reflectance** and the **transmittance** from these coefficients. The reflectance R is defined as the ratio between the incident intensity I_i and the reflected intensity I_r, or $R \equiv I_r/I_i$. As is commonly known, the intensity can be derived from the electric field's amplitude via $I = |E|^2$ resulting in:

$$R_p \equiv \frac{I_{rp}}{I_{ip}} = \left|\frac{E_{rp}}{E_{ip}}\right|^2 = |r_p|^2, \qquad R_s \equiv \frac{I_{rs}}{I_{is}} = \left|\frac{E_{rs}}{E_{is}}\right|^2 = |r_s|^2. \tag{3.14}$$

To calculate light transmittance, it is necessary to consider the relationship $I = N|E|^2$, along with the change in cross-sectional areas between the incident and transmitted media. This change, which results from the refractive index difference, can be determined using $\cos\theta_t/\cos\theta_i$. Combining these factors, we obtain

$$T_p \equiv \frac{I_{tp}\cos\theta_t}{I_{ip}\cos\theta_i} = \left(\frac{N_t\cos\theta_t}{N_i\cos\theta_i}\right)\left|\frac{E_{tp}}{E_{ip}}\right|^2 = \left(\frac{N_t\cos\theta_t}{N_i\cos\theta_i}\right)|t_p|^2, \tag{3.15}$$

$$T_s \equiv \frac{I_{ts}\cos\theta_t}{I_{is}\cos\theta_i} = \left(\frac{N_t\cos\theta_t}{N_i\cos\theta_i}\right)\left|\frac{E_{ts}}{E_{is}}\right|^2 = \left(\frac{N_t\cos\theta_t}{N_i\cos\theta_i}\right)|t_s|^2. \tag{3.16}$$

Since the general equations for p- and s-polarization are the same, differing only in the

Fresnel coefficients used, the formulas for reflectance R and transmittance T can be summarized as follows:

$$R = |r|^2 \qquad \text{and} \qquad T = \frac{N_t \cos\theta_t}{N_i \cos\theta_i}|t|^2. \tag{3.17}$$

In the case where $k > 0$ the relation $R+T < 1$ holds. The missing part is the **absorption** A, which can be calculated as follows:

$$A = 1 - R - T. \tag{3.18}$$

3.4 Optical Interference in Thin Layers

Interference is a fundamental phenomenon observed when two or more waves superimpose, leading to regions of constructive and destructive interference. Constructive interference occurs when the phase difference between the waves is an integer multiple of 2π, resulting in the amplitudes of the waves reinforcing each other. Conversely, destructive interference happens when the phase difference is an odd multiple of π, causing the waves to cancel each other out. In multi-layer systems, light can be reflected at a lower layer and recombine with light reflected from an upper layer. In layers that are a lot larger than the wavelength of light, the light can not be easily assumed to be monochromatic and coherent anymore which prevents interference [10]. In the case of PMTs one needs to consider that the photocathode layer has a **thickness** d of only about 20 nm, whereas the light that shall be detected usually ranges between 300 nm and 700 nm. A simplified system, which will be used to demonstrate the calculation of phase difference with a thin layer, is shown in Figure 3.5.

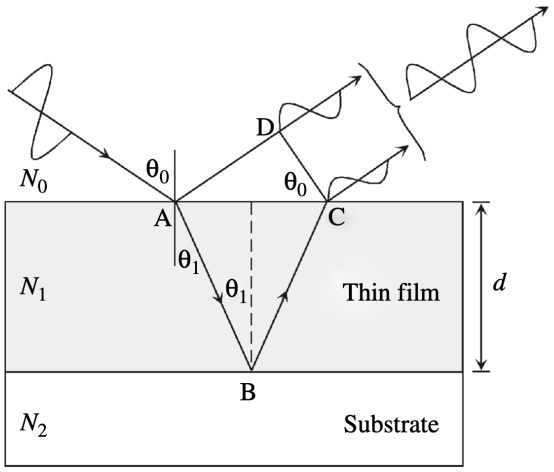

Figure 3.5: Illustration of light interference involving to a thin layer at an oblique incident. Figure taken from [16].

To calculate the phase difference one needs to compare the path lengths of the primary wave (reflected at point A and passing through point D) against the path length of the part that is transmitted at point A, reflected at point B and then transmitted at point C. In other words we compare the distance $\overline{AD}$ to the distance $\overline{AB} + \overline{BC}$. When expressing the electromagnetic wave as $E = E_0 \exp[i(\omega t - K_0 x + \delta)]$, K_0 is the propagation number in the first layer and the position is given by x. Therefore the phase change of the reflected wave from A to D by $K_0\overline{AD}$. Similarly, the phase change for the secondary part to be $K_1(\overline{AB} + \overline{BC})$), here K_1 is the propagation number inside the thin layer, which differs from K_0 only through the complex refractive index of the material, since $K = 2\pi N/\lambda$ and the wavelengths stays constant. Combining this, one can now

describe the phase difference as

$$\alpha = \frac{2\pi N_1}{\lambda}(\overline{\mathrm{AB}} + \overline{\mathrm{BC}}) - \frac{2\pi N_0}{\lambda}\overline{\mathrm{AD}}. \tag{3.19}$$

Analyzing the geometry of the paths inside the system, one can find a few trigonometric relations that allow to simplify the equation further:

$$\overline{AD} = \overline{AC}\sin\theta_0, \quad \overline{AC} = 2d\tan\theta_1, \quad \overline{AB} = \overline{BC} = d/\cos\theta_1 \tag{3.20}$$

and of course Snell's law. Together one finds

$$\overline{\mathrm{AD}} = 2d\,\frac{\sin^2\theta_1}{\cos\theta_1}\,\frac{N_1}{N_0}, \tag{3.21}$$

which can be reinserted into equation 3.19 to get

$$\alpha = \frac{4\pi d N_1}{\lambda}\left(\frac{1-\sin^2\theta_1}{\cos\theta_1}\right) = \frac{4\pi d N_1}{\lambda}\cos\theta_1. \tag{3.22}$$

The total phase variation of the secondary wave from point A to C indicates that the wave propagates through the depth of the layer twice. It is often more convenient to analyze the phase variation for a single trip from one interface to the other in any direction. Thus, the phase variation is defined as $\beta = \alpha/2$, also known as the **film phase thickness**

$$\beta_1 = \frac{2\pi d}{\lambda}N_1\cos\theta_1. \tag{3.23}$$

This process can happen multiple times, since a part of the wave transmitted at point C will also be reflected back into the medium and so on. This leads to a chain of Fresnel coefficients that define the ratio of the wave that is reflected or transmitted at any interface. An optical model visualizing this system is shown in Figure 3.6. The figure illustrates the necessity of tracking the Fresnel coefficients at each interface to predict the amplitude coefficients leaving the thin layer. At each reflection or transmission, the Fresnel coefficient of the respective interface is multiplied by the previous ones. If the wave passed the thin layer, a phase variation β is added into the waveform's amplitude in the form of

$$\exp[i(\omega t - Kx + \delta)] \Rightarrow \exp[i(\omega t - (Kx - \beta) + \delta)] \tag{3.24}$$

$$= \exp[i(\omega t - Kx + \delta)]e^{i\beta}, \tag{3.25}$$

where it is important to note, that due to the definition of the complex refractive index with a positive extinction coefficient $i\beta$ has a positive real part. To calculate the combined amplitude coefficients r_{012} and t_{012}, one needs to add an infinite sum of coefficients

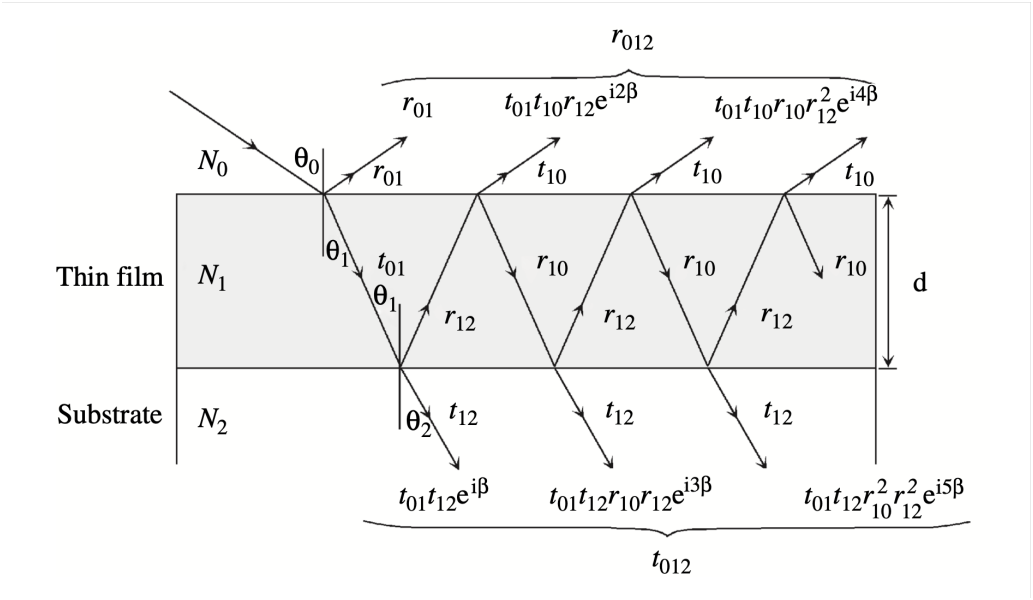

Figure 3.6: Optical system with a thin layer showcasing the Fresnel coefficients at several points. The total amplitude coefficients are the products of the ones from previous interfaces while r_{012} and t_{012} are the sum of the individual beams. Figure modified from [16].

respectively. Starting with the reflection amplitude coefficients, this would amount to

$$r_{012} = r_{01} + t_{01}r_{10}r_{12}e^{2i\beta_1} + t_{01}t_{10}r_{10}r_{12}^2e^{i4\beta_1} + \cdots \tag{3.26}$$

$$= r_{01} + t_{01}t_{10}r_{12}e^{2i\beta_1} \cdot \sum_{n=0}^{\infty} r_{12}r_{21}e^{2ni\beta_1} \tag{3.27}$$

$$= r_{01} + \frac{t_{01}t_{10}r_{12}e^{2i\beta_1}}{1 - r_{12}r_{21}e^{2i\beta_1}} \tag{3.28}$$

$$= \frac{r_{01} + r_{12}e^{2i\beta_1}}{1 + r_{01}r_{12}e^{2i\beta_1}}, \tag{3.29}$$

where the amplitude coefficients were interchanged using formula 3.13 as well as the geometric series

$$a \cdot \sum_{n=0}^{\infty} x^n = \frac{a}{1-x}, \quad x < 1. \tag{3.30}$$

To calculate the transmission amplitude coefficients one can proceed in a similar way by starting with

$$t_{012} = t_{01}t_{12}e^{i\beta_1} + t_{01}t_{12}r_{10}r_{12}e^{i3\beta_1} + t_{01}t_{12}r_{10}^2r_{12}^2e^{i5\beta_1} + \cdots, \tag{3.31}$$

apply the same rearrangements and the geometric series and one obtains

$$t_{012} = \frac{t_{01}t_{12}e^{i\beta_1}}{1 + r_{01}r_{12}e^{2i\beta_1}}. \tag{3.32}$$

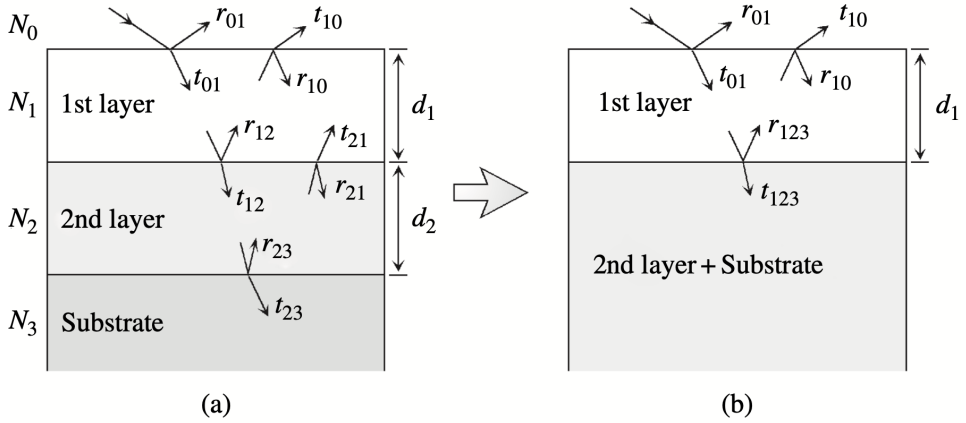

Figure 3.7: A four-layer optical system. In the context of a PMT-system N_0 would be air, N_1 glass, N_2 the photocathode and N_3 vacuum. Figure taken from [16].

Following this for a three-layer system the reflectivity and transmittance can be calculated applying equation 3.17 as follows:

$$R_{012} = |r_{012}|^2 \quad \text{and} \quad T_{012} = \frac{N_2 \cos\theta_2}{N_0 \cos\theta_0} |t_{012}|^2. \tag{3.33}$$

The photomultiplier system consists of not three, but four layers: the cover of the PMT is a "thick" glass layer, followed by a "thin" photocathode layer, and then a vacuum. Outside the PMT is the pressure vessel of the mDOM, which is filled with gel. However, for the purpose of the measurements in this work, we assume the presence of air instead. A four layer system is shown in Figure 3.7 (a). To calculate the amplitude coefficients of the entire system, one needs to start bottom up and calculate the amplitude coefficients of a three layer system consisting of the layers 1, 2 and 3 under the use of formulas 3.29 and 3.32 (one needs to adjust the indices accordingly), which results in r_{123} and t_{123}, which can then be reinserted into the same formulas as the amplitude coefficients of the new "bottom" layer, which would result in the amplitude coefficients of the entire system

$$r_{0123} = \frac{r_{01} + r_{123} e^{i2\beta_1}}{1 + r_{01} r_{123} e^{i2\beta_1}} \tag{3.34}$$

$$t_{0123} = \frac{t_{01} t_{123} e^{i\beta_1}}{1 + r_{01} r_{123} e^{i2\beta_1}}. \tag{3.35}$$

The total reflectance and transmittance of the system can then be obtained according to [17]:

$$R_{0123} = R_{01} + \frac{R_{123}(1 - R_{01})^2}{1 - R_{01} R_{123}} \quad \text{and} \quad T_{0123} = \frac{T_{123}(1 - R_{01})}{1 - R_{01} R_{123}}, \tag{3.36}$$

which also corresponds to the probability of a single photon that reaches the glass layer to be either leaving the PMT reflected back into air or transmitted into the vacuum. The

remaining intensity is absorbed according to

$$A_{0123} = 1 - R_{0123} - T_{0123}, \tag{3.37}$$

however this includes absorption in any layer. A photoelectron though can only be emitted if the photon is absorbed inside the photocathode layer.

4 Geant4 Simulation

The IceCube collaboration employs a variety of simulations during the design of their next generation of sensors, such as the mDOM. For an experiment of this magnitude, it is crucial to understand every detail about the detection process, the acquisition of raw data, and all intermediary steps, which is why simulation is used extensively for prototyping and characterization of next-generation optical modules. For the mDOM, a highly sophisticated **Geant4** simulation has been developed and refined through numerous works, notably by [2], [18], and [14] that further evolved into the OMSim project [19]. Among other applications, OMSim is useful for various physical case studies, such as calculating the effective area of optical modules, simulating radioactive decays in modules, or supernova studies with multi-PMT optical modules.

Geant4 (formed from "**GE**ometry **AN**d **T**racking") is a versatile simulation framework written in C++ that was developed at CERN and KEK. It utilizes Monte Carlo methods to simulate the passage of particles through matter, predicting interactions and energy depositions with high accuracy [20]. Widely used in particle physics, Geant4 provides a comprehensive library of physical interactions, including electromagnetic, hadronic, and optical processes. Its modular design allows for customization and extension, making it an essential tool for researchers to model complex experimental setups and optimize sensor designs.

Geant4 specializes in modeling three-dimensional detector layouts from basic geometric bodies like cubes, spheres etc. that can be assigned with properties like state, density, refractive indexes or absorption lengths for different wavelengths. Different particles can be emitted - for example from point sources - and propagated through the detector. On its way Geant4 tracks the particle and considers different interactions resulting in a possible change in trajectory, decay or absorption. This work is focused on optical processes mostly but is still embedded into an existing framework that is able to handle a variety of different particle interactions.

4.1 Photon Simulation

Although the simulation of the mDOM is capable of handling many different physical processes using different particles like gammas, electrons, ions and alpha particles, this simulation only involved simulation of photons to focus specifically on optical effects at interfaces. A Geant4 simulation **run** begins with the generation of an **event** from a source. These events follow a **track** until they interact with the detector geometry, where a **step** occurs. The potential physical interactions are defined in a **physics list**, which can be populated using the existing library of Geant4. In this work, the processes relevant for optical photons were selected, which can be seen in the following list:

- **G4OpAbsorption**: handles absorption inside a medium based on mean free path

- **G4OpBoundaryProcess**: handles optical processes like reflection and transmission at medium interfaces
- **G4OpRayleigh**: handles Rayleigh scattering
- **G4OpMieHG**: handles Mie scattering

The Geant4 class **G4OpBoundaryProcess** is particularly important in this context, as it handles reflection and transmission at interfaces. Prior to this work, the Geant4 simulation used by the Münster IceCube team to simulate the mDOM did not account for the optical impact of thin layers on the reflection and transmittance of a PMT. In any case where a photon reaches an interface with a different medium, Geant4 assesses the type of boundary encountered by the photon. It then selects the corresponding boundary process to calculate the probabilities of reflection, transmission into the next medium, or absorption. Each of these outcomes has distinct implications for the particle: in the case of reflection, the momentum vector is adjusted according to the law of reflection; in the case of transmission, it is adjusted according to Snell's law. In the case of absorption, the particle's track is terminated, potentially resulting in a detection.

A critical point in this work was the implementation of thin layer optics into the existing G4OpBoundaryProcess class. While the class was already capable of calculating photon trajectories through different media, it was not able to correctly handle optical phenomena at thin layers as described in Chapter 3. It is important to note that Geant4 does not simulate interference. This is by design, as Geant4 simulates each photon individually and their interactions are independent from each other. To circumvent this issue, the photocathode layer (the thin layer), that was previously modeled as a three-dimensional, 20 nm thick volume, was reduced to a virtual boundary that could be defined in between any two other volumes. While implementing this change, the detector geometry was also simplified to test if the results align with theoretical expectations. To be able to compare to the theoretical expectation described in Chapter 3, the optical system was simulated as a stack of four layers, as illustrated in Figure 4.1.

The first layer is air, as this will be the surrounding medium in the experimental validation of the simulation. Following this is the glass layer, which constitutes the outer shell of the PMT. This is succeeded by the thin photocathode layer, which is applied onto the inside of the glass. The third layer is the photocathode, which in Figure 4.1 is still visible, but in the final simulation reduced to only a boundary in between the surrounding layers, but assigned with a virtual thickness. PMTs are evacuated, making the fourth medium vacuum. From an optical perspective, air and vacuum can be considered similar, if not identical, as they share almost the same refractive index. As mentioned previously, the photocathode layer was modified to act as the boundary between the glass

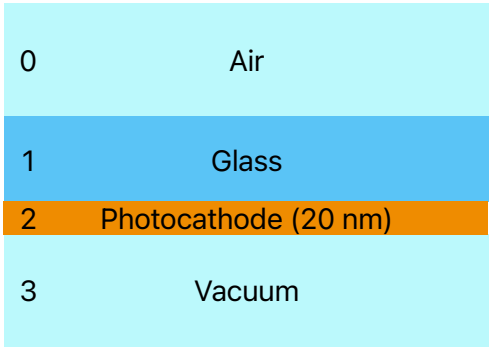

Figure 4.1: Visualization of the PMT-like four layer system. The photocathode is the "thin" layer.

and the vacuum layer.

Figure 4.2 shows a Geant4 visualization of the geometry in use: at first, a `World` is defined to encapsulate the detector. The world is assigned the material properties of air, thus also serving as the first layer. Within this world, two cuboids are placed: one with the properties of a common borosilicate glass, and another beneath it designated as air. The photocathode was defined as the interface between the two volumes with the attribute `coated`. This attribute activates the custom function `PhotocathodeCoated()` written in the framework of this thesis, when a photon crosses the boundary. In Geant4 a coating can be assigned with different properties like a refractive index, an absorption length or a (virtual) thickness. Additionally, invisible detectors are placed above and below the simulation setup to count the number of photons that are reflected or transmitted, respectively. In the visualization the photons are made visible as orange tracks. In yellow one can spot interaction points, where photons interacted with the materials it traversed or were detected by the detectors at the top and bottom. It is important to note, that the thin layer interaction has to work from both directions, since internal reflections in the PMT may reflect back through the photocathode layer to the outside of the PMT and by doing so trigger `PhotocathodeCoated()` "in reverse". This is validated in Chapter 6.

A typical simulation run would start by defining the initial properties of the photons, like the wavelength, the distance of the source from the worlds center, the incident angle and the number of events. For this work the wavelength of the photons was kept at 480 nm, since that will be the wavelength used in measurement. The number of events in these setups amounted to 10^6 per incident angle, that was successively shifted in steps of 1°

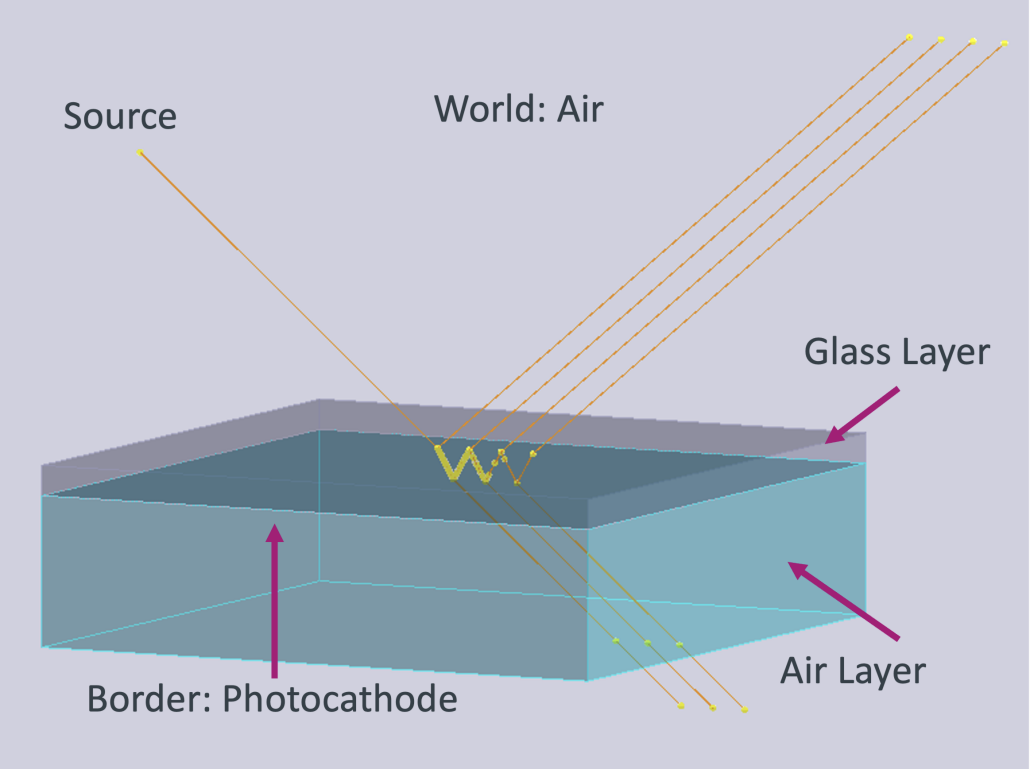

Figure 4.2: Visualization of the simulation setup consisting of the surrounding world, the glass layer, the vacuum layer and the (not visible) photocathode-boundary. In orange are the tracks of the photons (10^6 events here) and in yellow the points were an event occurred.

from 0° to 90°. An angle of 0° corresponds to the normal on top of the glass layer, where the point of contact of both is the worlds center.

When a photon reaches the glass, function already included in Geant4 calculates the probability of reflection or transmission depending on the Fresnel coefficients of the air-glass interface. If reflected, a detector placed above the system will count it. If transmitted, Geant4 uses Snell's law to calculate the new trajectory inside the new medium. Once transmitted and inside the glass, an absorption can happen at any time according to the absorption length of the glass, as can be seen for example in Figure 4.2 as the yellow dots inside the glass layer. If the photon reaches the end of the glass layer and meets the boundary with the air layer, the `PhotocathodeCoated()` function will trigger and interpolate the complex refractive indices at the current wavelength from the absorption lengths of the three materials that make up the incident medium, the boundary and the transmitted medium. Using those it calculates the film phase thickness of the boundary to calculate the Fresnel coefficients of the three-layer system surrounding the boundary using Equations 3.29 and 3.32.

It should be noted, that the consequent handling of complex refractive indices results in complex results for the angle of transmission from Snell's law. Before this work Geant4 did not use the imaginary parts of said angles to determine a particles trajectory, even though the necessary groundwork seems to exist in some functions. This resulted in photons arriving at the thin layer with a purely real incident angle, which is not the case if one considers the - admittedly small - extinction coefficient of glass - the layer the photon just traversed. This makes the handling of a particles trajectory quite delicate, since an imaginary angle does not physically exist in our three dimensional space, but its mathematical existence changes the physical angle, phase and probability of reflection or transmission of the electromagnetic wave for subsequent interfaces [21]. To avoid this inaccuracy, an additional routine was implemented that keeps track of the last layers[1] a particle has passed through (since Geant4 in the usual case only saves information necessary to determine the next step of a particle, but not its history). The information about the previous history of the photon can then be used to retroactively calculate the complex angle of its trajectory and the resulting implications for the calculations of the reflectance, transmittance and absorption of the three-layer system around the thin layer according to Equations 3.33. It turns out, that the expected results for total reflectance and transmittance of the system change not by much, but still significantly, depending on how rigorously complex refractive indices are used throughout the simulation.

Another thing that needs to be pointed out here is, that in a three-dimensional thin layer the incident point - where the photon meets the thin layer - would not be the same as where a photon, that was reflected inside the thin layer and transmitted back into the glass layer, starts the new trajectory inside said glass layer. This is illustrated in Figure 3.5 as the distance $\overline{AC}$. This shift had to be neglected due to the two-dimensional thin layer in this approach, that only has a virtual thickness but no physical in the setup. Any possible internal reflections inside the thin layer are accounted for by the equations used before and a large enough sample size of events. If the photon is absorbed, the track ends inside the thin layer and if it is transmitted, it will propagate through the air

[1] (for this purpose: the last two layer

layer and be detected and counted at the bottom detector. Only photons that reach the detectors above or below the sample, or those absorbed at the boundary are counted for later evaluation. After a particles track ends at any points, the next event is generated. The whole process works similar if the photon is coming from below the sample, just in reversed order. It will be later shown that this procedure converges well towards the theoretical reflectance and transmittance of the whole system with interfering photons as described in Chapter 3.

5 Optical Measurements of Reflectance and Transmittance

A new method to simulate the reflectance and transmittance of an optical system, including a thin layer, was introduced in Chapter 4. To validate the theoretical considerations and their implementation in a Geant4 simulation, a series of optical measurements were performed. These measurements were conducted on samples that mimic the simulation setup and possess optical properties similar to those of a photocathode. The production process and initial characterization using a commercial setup will be explained in the following two sections. Subsequently, the reflection and transmission measurements were conducted using a modified version of the ellipsometer setup commissioned in [22], enabling the measurement of reflectance and transmittance of a sample using a 480 nm laser.

5.1 Production of the Samples at CeNTech

As mentioned in Section 2.5 the photocathode of the PMTs used for the mDOM are made of Potassium Cesium Antimonide (KCsSb). There are two primary reasons why it was not feasible to conduct measurements on samples made from the photocathode material itself. First, the exact material composition is a closely guarded trade secret of the manufacturer, *Hamamatsu Photonics*. Second, and more critically, KCsSb is highly susceptible to oxidation upon exposure to air, making it impossible to perform the desired measurements in air. This is also why PMTs are evacuated. Previous ellipsometric measurements have determined the refractive index of the photocathode to be approximately $N_{PC} = 2.54 + 1.13i$ [23] at a wavelength of 400 nm. Based on this information, two alternative materials, **Chromium (Cr)** and **Palladium (Pd)**, were selected, with the following refractive indices [24, 25]:

Refractive Indices of Selected Materials

- **Chromium**: $N_{\mathrm{Cr}} = 2.69 + 4.71i$
- **Palladium**: $N_{\mathrm{Pd}} = 1.61 + 3.64i$.

The refractive indices are literature values at a wavelegth of 480 nm.

The samples were produced in cooperation with the Center for Nanotechnology Münster (CeNTech). As a substrate, common microscope slides made out of borosilicate glass were used. These were placed in a commercial Multi Hearth Evaporator [1] manufactured for

[1] Beamtec Electron Beam Evaporator EBM-6II

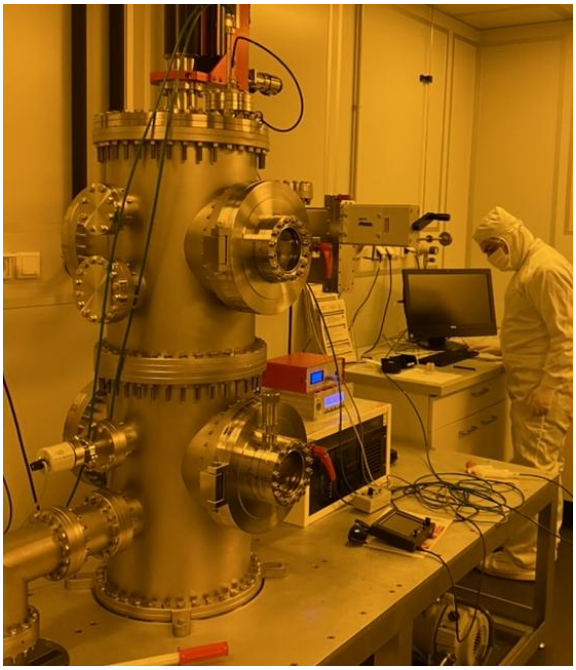

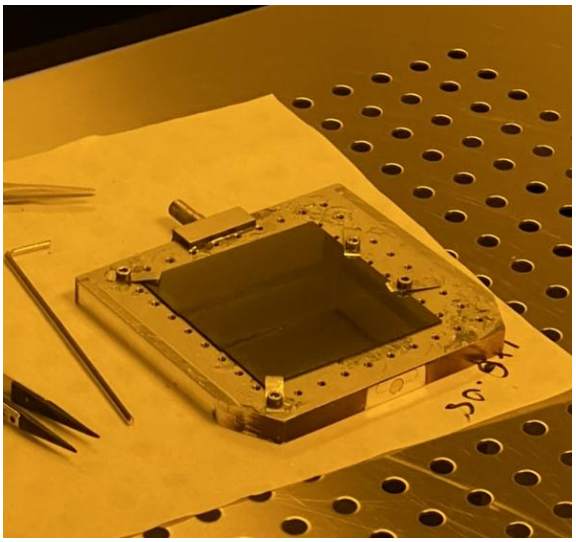

Figure 5.1: Left: Picture of the electron beam evaporator and a supervising engineer of CeNTech. Right: Picture of the three finished samples after deposition.

Electron Beam Physical Vapor Deposition (EB-PVD) and located in a cleanroom environment at CeNTech [26, 27]. A picture of the device is shown on the left in Figure 5.1. During EB-PVD an electron beam targets a sample of the material to be deposited under high vacuum. The beam detaches atoms from the sample that become gaseous and settle on the substrate, where they form a uniform solid layer [28]. Two runs were performed - one for each material - that produced three samples each. The samples were arranged next to each other in a holding structure as can be seen in the right picture in Figure 5.1.

5.2 First Characterization of the Samples at SoN

In the course of preparing the samples at CeNTech, it was also possible to take a first series of measurements at the **Center for Soft Nanoscience (SoN)**. The Nanochemistry zone cleanroom environment at SoN features a ellipsometer[2] that is shown in Figure 5.2.

The ellipsometer came pre-equipped with analysis software for a range of sample materials including Cr and Pd, which allowed measurement of sample thickness and refractive index at a fixed angle across a range of wavelengths

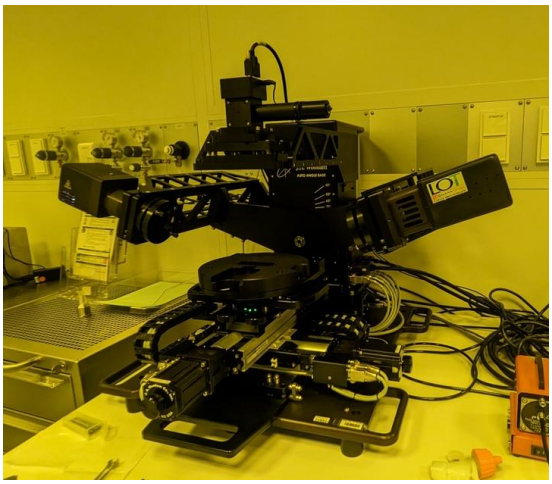

Figure 5.2: Picture taken of the Woolam M-2000 ellipsometer in the Nanochemistry zone at SoN.

[2]Woolam M-2000

Table 5.1: Thickness Measurements of Chromium (Cr) and Palladium (Pd) samples

Material	Sample	Thickness (nm)
Cr	Cr1	19.48 ± 0.140
	Cr2	19.18 ± 0.132
	Cr3	19.46 ± 0.145
Pd	Pd1	22.80 ± 0.072
	Pd2	22.66 ± 0.086
	Pd3	22.62 ± 0.092

[29, 30]. The results of the measurement of the thickness are presented in Table 5.1. The ellipsometer measured the thickness of each sample at a single spot, chosen to be as close to the center as possible by eye and with a built-in ruler with millimeter accuracy. As shown in the table, the samples of each material have very similar thicknesses, as expected from the same deposition run. The slight differences in thickness beyond the margin of error could be due to non-uniform deposition, handling, or transport, where the samples might have been touched or slightly dented. Directly following the measurement of the thickness the ellipsometer measured the refractive index and extinction coefficient of each sample at the same spot where the thickness was measured before. The ellipsometer was set to a constant angle of 65° and measured both coefficients at varying wavelengths from 370 nm to 1000 nm. The results are shown for Cr in Figure 5.3 and for Pd in Figure 5.4. Both plots feature a vertical line at 480 nm, which is the wavelength of the laser used later in the measurements.

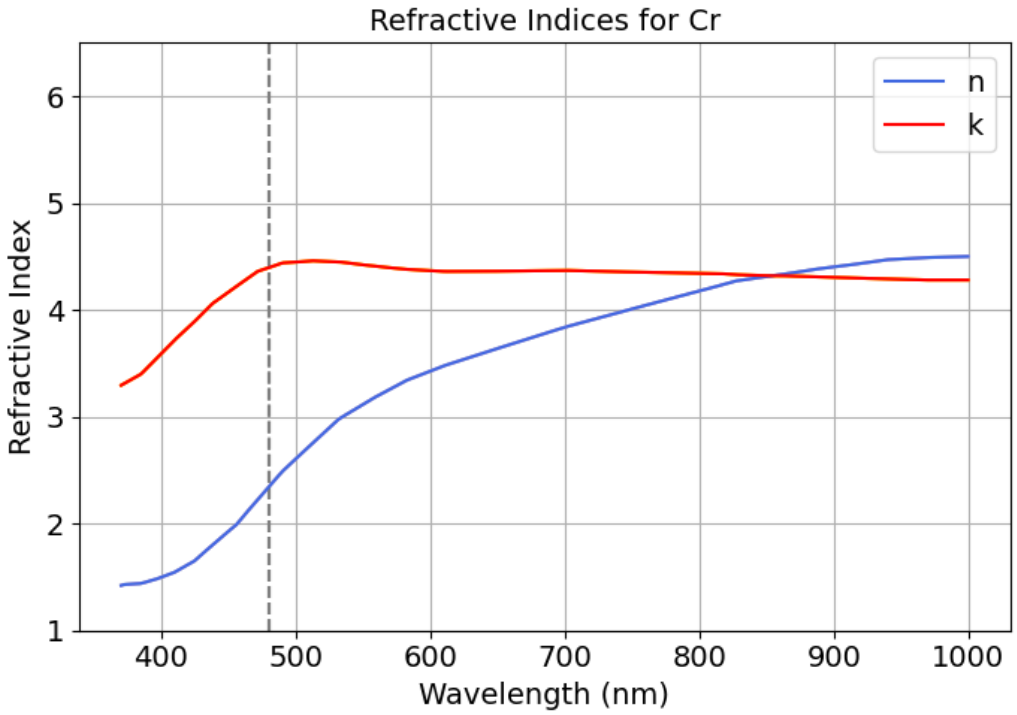

Figure 5.3: Real (n) and imaginary (k) part of the refractive index of Chromium measured at SoN. The vertical line is at a wavelength of 480 nm.

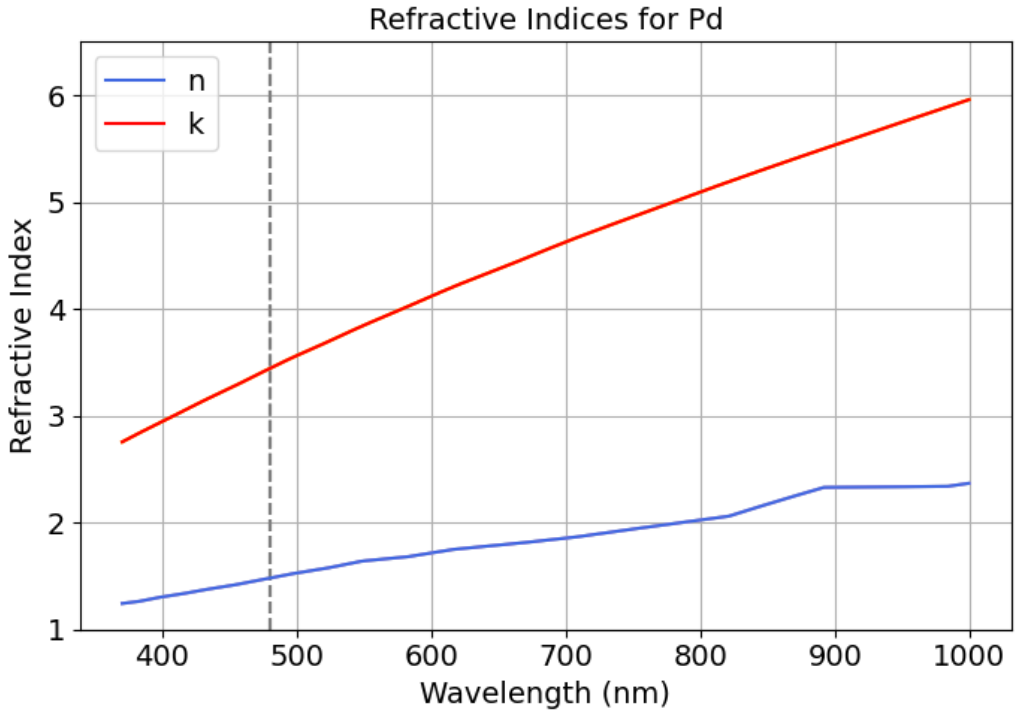

Figure 5.4: Real (n) and imaginary (k) part of the refractive index of Palladium measured at SoN. The vertical line is at a wavelength of 480 nm.

The ellipsometer's closest measurement to this wavelength was at 481.1 nm. At this point, the measured refractive indices were as follows:

Refractive Indices measured at 481.1 nm at SoN

- **Chromium**: $N_{\mathrm{Cr}} = 2.33 + 4.39i$
- **Palladium**: $N_{\mathrm{Pd}} = 1.48 + 3.44i$.

The measured refractive indices are approximately 10% lower than the literature values reported in [24] and [25]. The exact cause of this discrepancy is unclear, as the procedures used by the commercial setup and software are not fully transparent. Additionally, the setup yielded identical values for each of the three samples of both materials, resulting in a single set of values for n and k in each plot of Figure 5.3 and 5.4. Consequently, these refractive index measurements should be considered with caution. However, this is not a significant concern, as these parameters will be remeasured using a different setup and method in the following chapter.

5.3 Measurement Setup for Reflectance and Transmittance

The setup used to measure the reflectance and transmittance of the samples is shown in Figure 5.5. During the measurements, the laboratory environment was maintained in darkness and at a temperature of 18 °C. It consists of several key components, each explained in detail below. The laser[3] emits an initial beam with a broad range of wavelenghts and is therefore connected to a monochromator[4] to select the wavelenght of interest. A monochromator acts as a bandpass filter and usually consists of a combination of prisms or optical grating to filter from a spectrum of wavelengths one single desired wavelength, which for the purpose of this work was 480 nm [31]. To ensure constant laser intensity during measurements, the laser was started the day before each measurement. A photodiode[5] was used to detect the intensity of the reflected and transmitted laser light. This photodiode was mounted on a moveable arm and connected to a picoamperemeter[6]. The sample was placed in a mounting bracket atop a rotation table[7] on a hexapod[8]. The hexapod enables to position the sample in x, y and z direction, as well tilting in three angular dimensions Θ_x, Θ_y and Θ_z. This is necessary to precisely align the laser to the normal of the sample in the rest position and to tilt the sample accurately in the plane of the laser and photodiode. To normalize the measured intensity at the photodiode, a second photodiode was placed orthogonal to the beam path before the sample, with a beamsplitter[9] diverting a well-defined fraction of the initial laser intensity to this second photodiode.

Using this setup, the laser was aimed at the center of each sample, and the reflected or transmitted beam was detected by the first photodiode. The transmittance measurements were conducted from both sides of the sample - which refers to weather the laser was pointed at the glass side of the sample or the thin layer made of Cr or Pd. The measurements of the reflectivity were done with the laser pointing towards the thin layer of the sample only. The hexapod stands on three legs with the movable arm of the first photodiode mounted in between, which allowed measurements of reflection only at incident angles ranging from 25° to 65° in one measurement run and from 63° to 90° in another. The data from these two runs were later merged, resulting in some overlap and duplicate measurements for a few angles. For transmittance measurements, angles from 0° to 90° were covered in a single run.

In reality the incident photon from Cherenkov radiation would always reach the PMT-glass first, which would correspond to measuring this setup with the glass side of the sample facing towards the laser. Still both orientations are important to understand, since back reflections inside the PMT that reach the photocathode would correspond to the material side of the sample facing the laser. Due to time constraints the reflection

[3] NKT Photonics SuperK Compact Supercontinuum Laser
[4] NKT Photonics LLTF Tunable High Contrast Filter
[5] Hamamatsu S2281
[6] Keithley 6482
[7] Standa 8MR151 - Motorized Rotation Stage
[8] PI H-820 6-Axis Hexapod
[9] Thorlabs BSN10

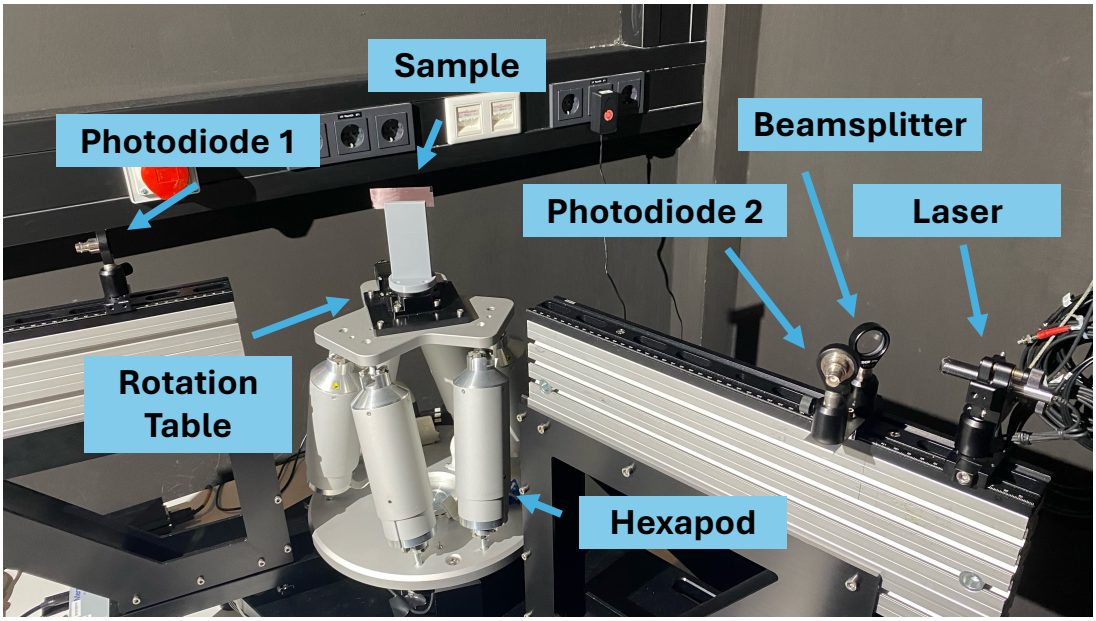

Figure 5.5: Picture taken of the measurement setup used for the measurements of reflection and transmission. Photodiode 1 can be manually moved on a rotation arm. Cables have been removed for clarity.

measurements could only be conducted in the "reverse" orientation with the material facing the laser. This orientation was chosen because it was predicted to exhibit more significant characteristics in the data.

However, accurately measuring intensity became increasingly difficult for angles above around 85° due to laser beam scattering. While the laser theoretically acts as a point source, in practice, its non-negligible diameter affects measurements at shallow angles. Problematic data points, where the laser did not hit the sample properly, will be discussed later. A schematic sketch of the measurement setup is shown in Figure 5.6.

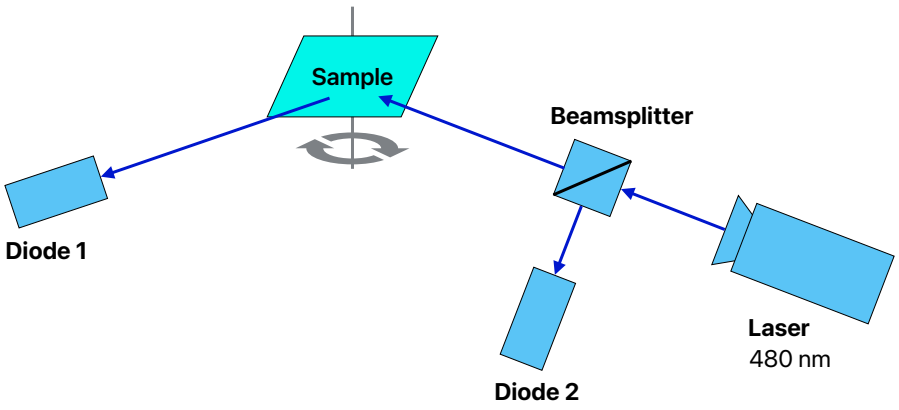

Figure 5.6: Sketch of the measurement setup used for the measurements of reflection and transmission. Diode 1 can be moved around the sample depending on the angle of refraction or transmission. Diode 2 is for reference.

5.4 Data Acquisition and Handling

For each angle a Python script was executed that reads out the intensity measured at the picoamperemeter one hundred times for both photodiodes. These values were saved together with the angle of incidence θ_i. Additionally, for each measurement run a background measurement was conducted for which the beam path was blocked. To infer the reflectance or the transmittance of the sample depending on the measurement, several processing steps were applied to the data: first, the measured intensities were averaged over all one hundred data points for each angle at both diodes. Afterwards the average background was subtracted. To interpret the output of the picoamperemeter, some known relations can be used [32]: such as the light divergence ratio at the beamsplitter which as characterized on a previous measurement. It is known that it does reflect $(9.27 \pm 0.05)\%$ of the total intensity of the laser to the second photodiode while transmitting $(89.4 \pm 0.4)\%$ of the total intensity towards the sample. Additionally, one needs to correct for slight difference in calibration between first and second photodiode, where it is known that for a constant intensity from the laser the relation $I_1/I_2 = 1.0117 \pm 0.0026$, where I_1 is the intensity measured at the first photodiode and I_2 the intensity measured at the second, holds. Further, the light reaching the sample has previously been characterized to consist of 95.6% unpolarized light as well of 4.4% partially polarized light, which again can be disassembled into 50.4% p-polarized light and 49.6% s-polarized light. For the error of I_1 and I_2 the standard deviation of each set of one hundred data points was assumed.

6 Analysis

In the following chapter, the results of the previously explained measurements are presented and compared to the theoretical expectations derived in section 3 as well as the Geant4 simulation that was described in chapter 4. The objective is to determine the complex refractive index and thickness of a thin film on various samples based on reflection and transmission measurements. All literature values for the complex refractive indices are given for a wavelength of 480 nm.

6.1 Theoretical Expectations: Three Layers

The calculation of the theoretical reflectance and transmittance of a sample varies based on the orientation of the sample — whether the laser hits the side of the glass or the thin layer first. Initially, the scenario where the laser hits the thin layer first is considered. In this case, since internal reflections in the glass are negligible towards interference inside the thin layer, the glass beneath the thin layer can be treated as a substrate for now, reducing the optical system to a three-layer model. This simplified system is illustrated in Figure 3.6 with the materials depicted in Figure 6.1 and their complex refractive indices listed in Table 6.1.

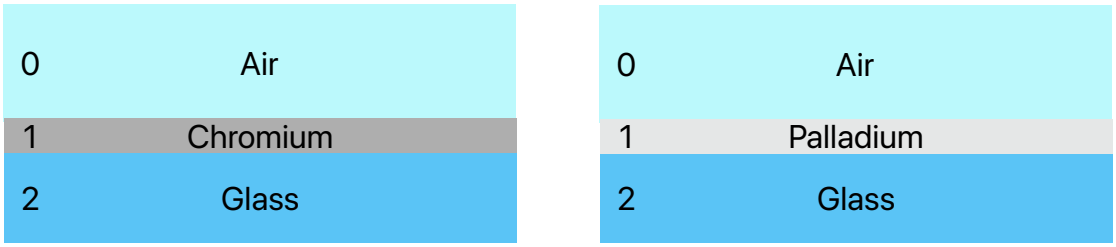

Figure 6.1: The three-layer systems that represent the samples used during the measurement. Cr and Pd are the thin layers in their respective optical system. The complex refractive indices of each material are given in Table 6.1.

Based on the calculations in Chapter 3 and using the complex refractive indices from Table 6.1, along with an assumed thin layer thickness of 20 nm, one can calculate R_{012}

Table 6.1: Literature values of the refractive indices for the three-layer system with different materials for the middle layer N_1. Values taken from [24, 25].

Layer	Material	Refractive Index
N_0	Air	$1.0003 + 0i$
N_1	Chromium	$2.69 + 4.71i$
N_1	Palladium	$1.61 + 3.64i$
N_2	Glass	$1.525 + 9.549 \times 10^{-8}i$

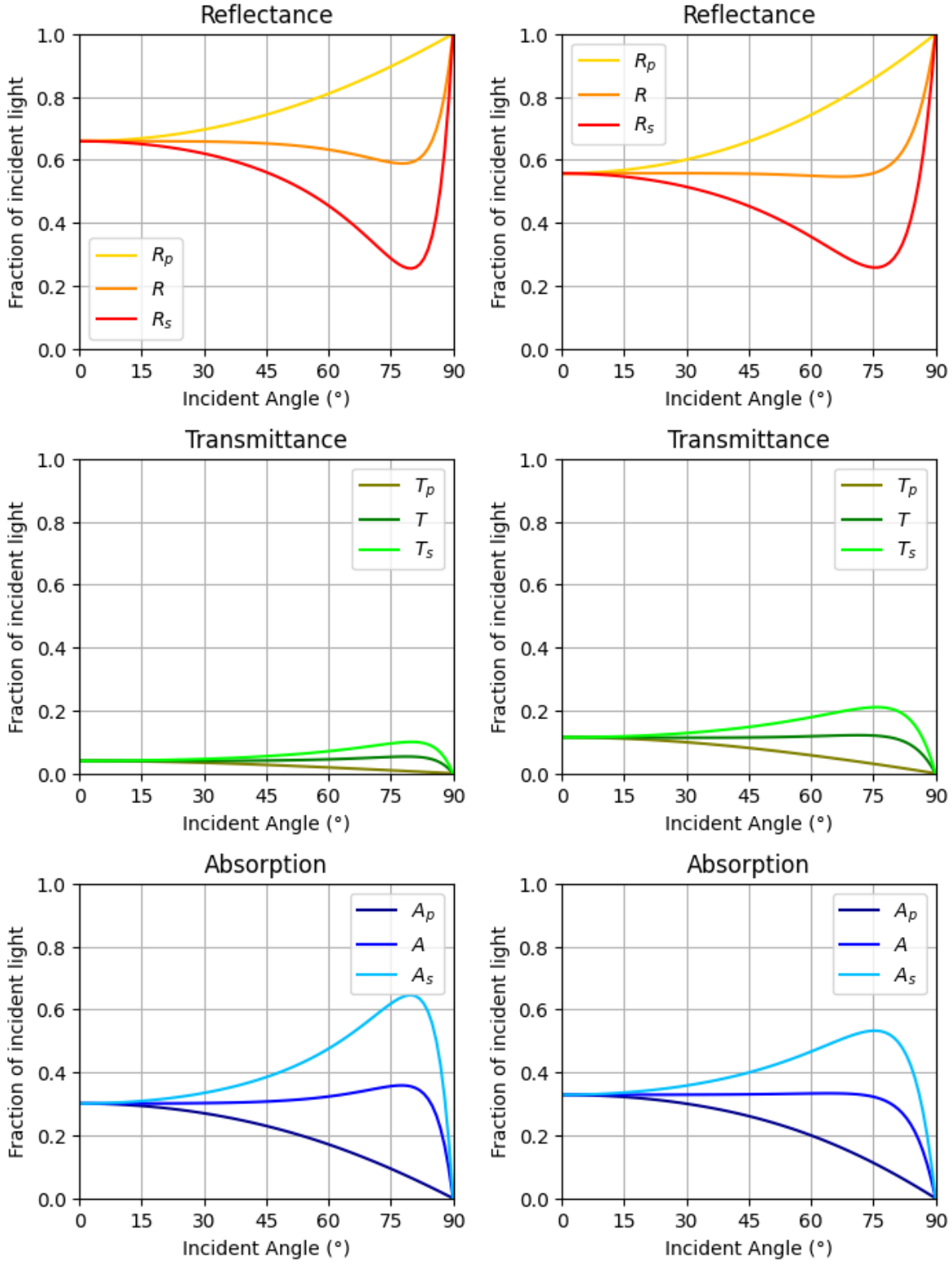

(a) Chromium **(b)** Palladium

Figure 6.2: Theoretical expectations for reflectance R, transmittance T and absorption A for s- and p-polarization as well as the average of both for a Cr-system in (a) and a Pd-system in (b) as introduced in Figure 6.1.

and T_{012} according to Equations 3.33 in p- and s-polarization at various incident angles and subsequently A_{012}. The laser light used for measurement is circularly polarized, meaning equal parts of p- and s-polarized light reach the sample. Figure 6.2 presents the theoretically expected values for reflectance, transmittance, and absorption for such an optical system using Cr in (a) and Pd in (b) as the sample material in the middle layer.

In Figure 6.2 each plot features the theoretically expected fraction of incident light that is either reflected, transmitted or absorbed by the sample, presented for both p- and s-polarization, as well as their average. In future plots that feature the theoretically expected values of measured variables, only the average of s- and p-polarization will be shown. This is to maintain clarity, as it is not possible to distinguish between the polarizations in the current measurement setup as the light is left unpolarized.

Several key observations can be made from these plots that will be recurring in future analyses. While the graphs for p- and s-polarization differ considerably in magnitude and shape, their average values remain approximately constant for reflectance, transmittance, and absorption at lower incident angles until around 40° to 45°. At that point, the reflectance of the Cr system dips slightly before quickly rising to 100% reflectance at 90°. A similar trend is observed for Pd, but it is much less pronounced. In contrast, the transmittance behaves oppositely. Starting significantly lower at around 4% for Cr and 11% for Pd. This difference in transmittance is easily understood when considering that Cr has a higher extinction coefficient than Pd, resulting in a much shorter absorption length. At very high angles above approximately 70° the transmittance increases a little bit, before dropping to 0 at 90°. The absorption is in both systems in the range of 33% for the most part of the spectrum. This parameter plays an important role in the detection efficiency of a PMT, since only a photon that is absorbed can produce a photoelectron - although the absorption in this case includes the absorption in the entire system including the glass and not only in the thin layer.

6.2 Theoretical Expectations: Four Layers

As previously mentioned in section 5.3 the usual case for a photon-PMT-interaction would be, that the photon reaches the glass of the PMT first and then - if transmitted - reaches the photocathode material afterwards. In this case the glass can no longer be considered a substrate, since it lies in the middle of the system, and the optical system of the measured samples enlarges to four layers, as illustrated in Figure 6.3.

In this case Equations 3.33 do not apply anymore and Equations 3.36 need to be used instead. These equations feature the film phase thickness β two times for different layers. Before it was straight forward to use the film phase thickness β_1 of the thin layer N_1 to calculate r_{012} and t_{012}. This is possible because even though the laser light is not perfectly monochromatic - which would be necessary for interference, the optical path length is short enough to be able to neglect any possible phase changes in the lasers waveform that would appear over time. This quasi-monochromatic light behaves therefore like monochromatic light in this environment. In literature this is referred to as the **coherent condition** and is relevant for $d \leq \mathcal{O}(\lambda)$ [16].

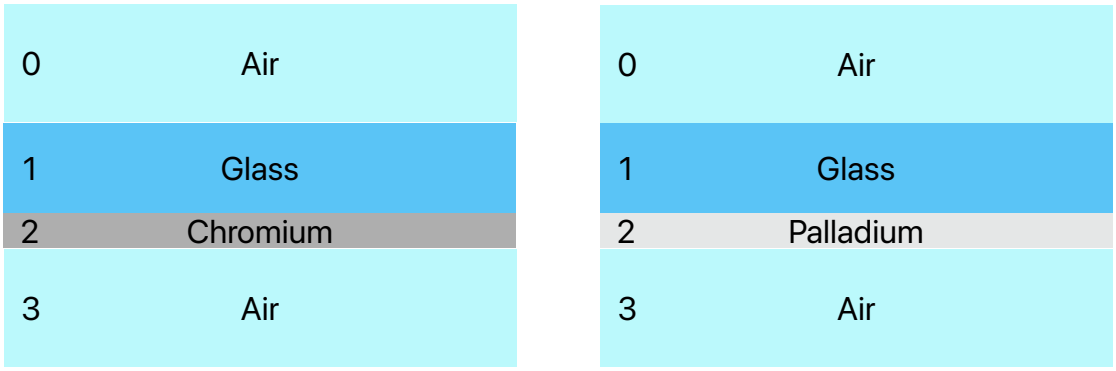

Figure 6.3: The four-layer systems that represent the samples used during the measurement. Cr and Pd are again the thin layers in their respective optical system. The complex refractive indices of the materials did not change.

In this four-layer optical system with the reflectance R_{0123} and the transmittance T_{0123}, β_2 appears for the thin layer N_2 inside r_{123} and t_{123}. Conversely, β_1 refers to the film phase thickness of the glass layer, that is N_1 here. The thickness d_1 of the glass layer is approximately 2 mm - the size of a common microscope slide. As this is much larger than the wavelength of the laser light, the light passing this layer can no longer be considered monochromatic (**incoherent condition**). To avoid introducing an interference effect that would only occur for perfectly monochromatic light, the corresponding factor is assumed $e^{i\beta_1} = 1$ ($\beta_1 = 0$), which would imply no effect from interference on the amplitude coefficients of the electromagnetic wave. Afterwards, when the light that has been transmitted through the glass layer reaches the thin layer, it can be considered quasi-monochromatic again for the previously stated reasons.

The theoretical expectations for the reflectance, transmittance and absorption of a four-layer system of the form as illustrated in Figure 6.3 are presented for both Cr and Pd in Figure 6.4. Again split into p- and s-polarization as well as their average.

One quickly sees, that on first impression the plots presented for the four-layer optical system in Figure 6.3 are very similar in general shape to the three-layer optical system in Figure 6.1. The most notable difference is the absence of the dip in the reflectance plot for Cr. Also p- and s-polarization do not diverge as much of each other as they did in the previous three-layer system. Besides the shape of the plots, the magnitude of some coefficient changed considerably: reflectance is lower by around 10% for both Cr and Pd, while absorption is equally higher, as transmittance did not change significantly. These are important characteristics to observe in the results of the simulation and the measurement.

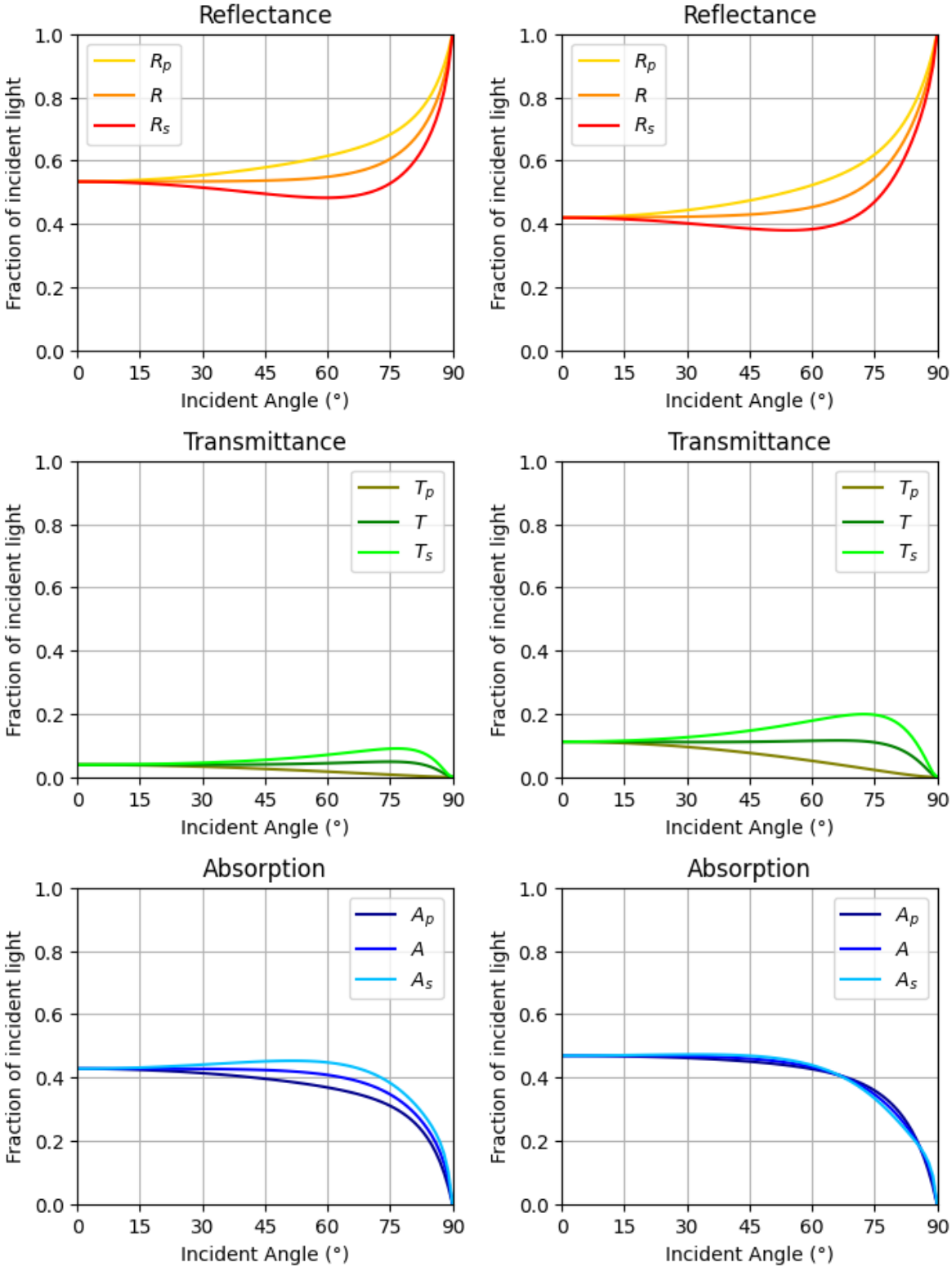

(a) Chromium **(b)** Palladium

Figure 6.4: Theoretical expectations for reflectance R, transmittance T and absorption A for s- and p-polarization as well as the average of both for a Cr-system in (a) and a Pd-system in (b) as introduced in Figure 6.3.

6.3 Evaluating Geant4 Simulation Results

During the implementation of the theoretical groundwork from Chapter 3 a few unique features of working with Geant4 have emerged that should be explained before presenting the final results of the simulation. In Geant4, each particle possesses only as much information of its surroundings as necessary to know the next step of its trajectory. As previously mentioned in Chapter 4, this is why, for example, interference is not included in Geant4's toolkit, since this would require information about separated events. This also means, that previously it was not possible to structure a function for the entire PMT-shell-system all at once, as an incident photon reaching the glass simply did not have the information of what lies beyond it. Instead, Geant4 calculates the probability of reflection or transmission at each interface and the probability of absorption at every step based on the medium's absorption length. A simulation of 10^5 events using Geant4's default `OMSimOpBoundaryProcess` class to simulate reflectance, transmittance and absorption for a Cr-sample is shown in Figure 6.5. For this simulation the Cr-layer was defined as a physical volume with a thickness of 20 nm. One quickly sees, that there is significant difference from the theoretical expectations presented in the previous sections for all three quantities.

To be able to circumvent this problem - not being able to address interference effects inside the thin layer - the same was made a two-dimensional border in between two different volumes instead as illustrated in Chapter 4 and the simulation was run again, otherwise unchanged from the front and back side of the sample.

Figure 6.6 shows the final R-, T- and A-results of the Geant4 simulation when using the

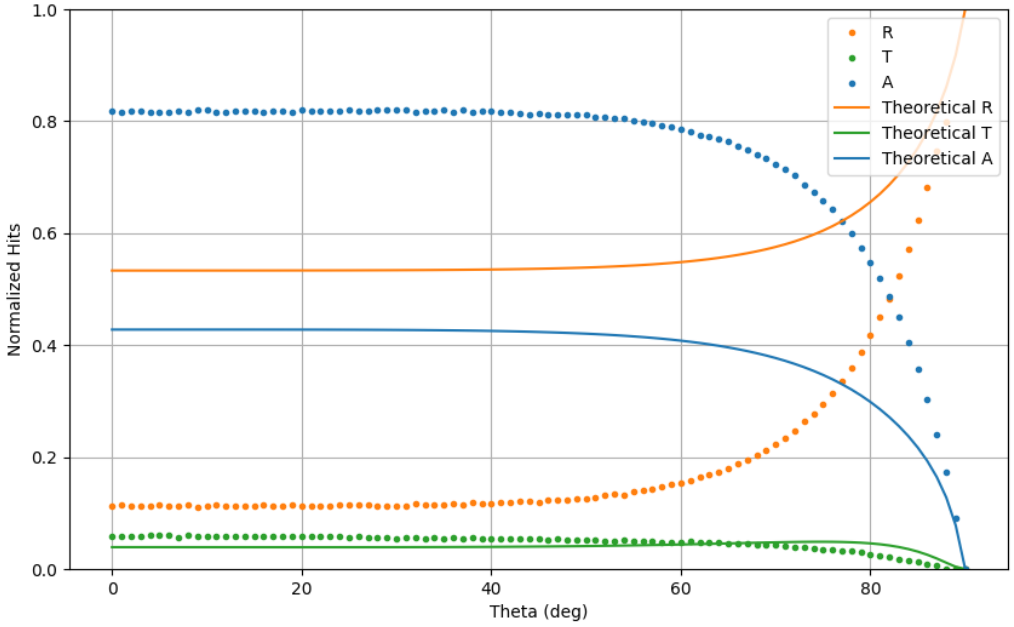

Figure 6.5: Results of a Geant4 simulation of 10^5 events hitting a Cr-sample from the glass side in a four-layer system without using thin-layer-optical functions, but defining the Cr-layer as a physical volume with a thickness of 20 nm instead.

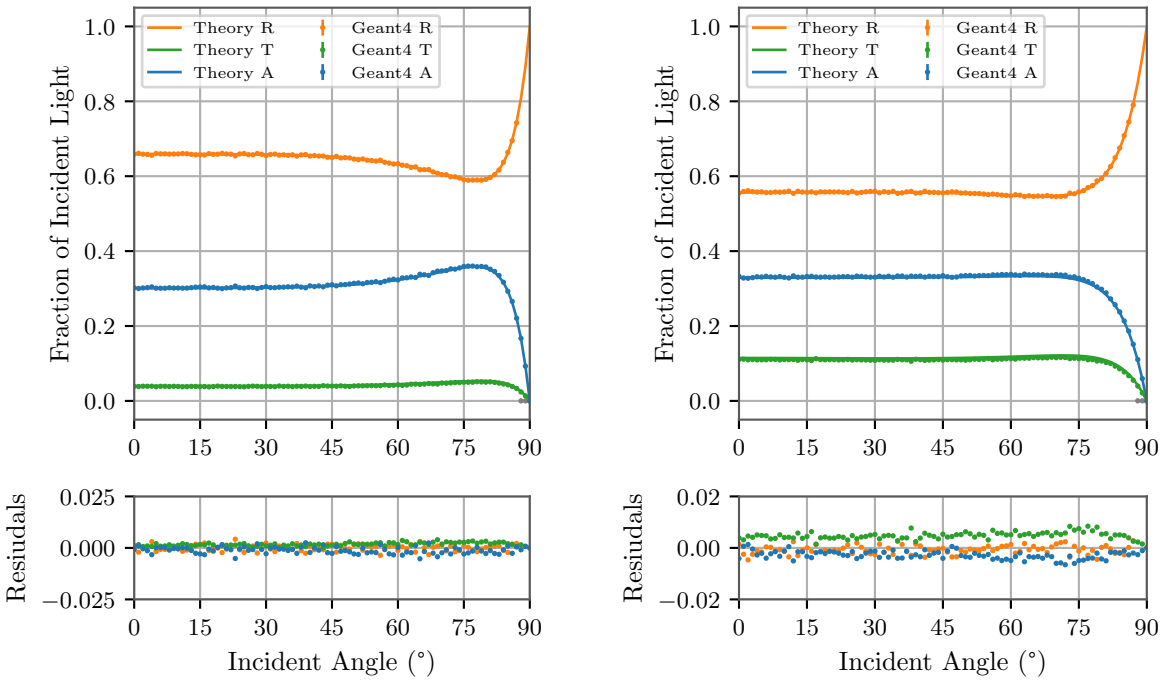

(a) air-**Cr**-glass

(b) air-**Pd**-glass

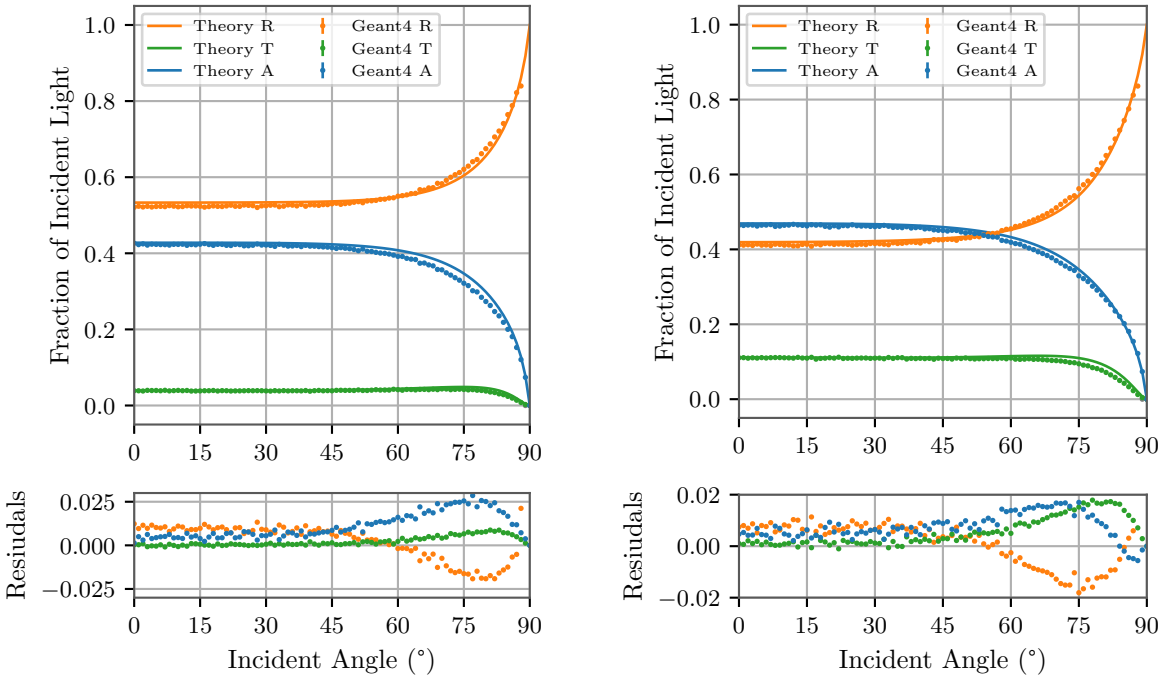

(c) air-glass-**Cr**-air

(d) air-glass-**Pd**-air

Figure 6.6: Results of Geant4 simulations of 10^5 events for both samples - Cr and Pd - with both sides facing the photon source compared the the theoretical results. Below each plot the absolute difference between simulation and theory is shown. Faulty points from simulating reflectance at high angles that did not hit the detector above are colored in grey.

literature values from Table 6.1. For each material the simulation was conducted in both orientations of the sample: the material facing the photon source, which corresponds to the three-layer system explained in Section 6.1, or the glass facing the photon source, which would correspond to the four-layer system from Section 6.2. These results are compared to the theoretical expectations of each value for each setup. Below each plot a residual diagram shows the absolute difference between simulation and theory. Also shown in grey are faulty measurement points from the reflectance measurement where the reflected photons did not hit the (not infinitely large) detector on the top side anymore, which happened at very steep angles. One can see that for the samples with the material facing the photon source the residuals show no underlying structure. The Geant4 simulation and theoretical expectations match completely. The simulation of the samples that face the source with the glass side also reflects the theoretical expectations well at angles up to 50°. Here on the other hand a slight structure forms, where the reflectance of the simulations exceeds the theoretical expectation. However the difference is relatively small at about 3% relative to each other at the highest point around 75°. This slight deviation is likely caused by the handling of complex angles in layers before the Cr- or Pd boundary in the four-layer model as explained above, since it does not appear in the orientation where the incident photons hit the Cr- or Pd boundary first and where the glass layer was treated as a substrate afterwards. It is assumed that the calculation of reflectance and transmittance at standard dielectric-dielectric interfaces in Geant4 treats the complex angles that continue into the calculation of Fresnel coefficients imprecisely, but it was not possible to recreate a theoretical scenario that would mimic this inaccuracy well enough to imitate the simulation results perfectly.

6.4 Evaluating R and T Measurement Results

In the following the results of the measurements of reflectance and transmittance are presented and compared to the respective theoretical models. Before delving into the results, the general approach for the analysis of all measurements will be explained. Measurements of reflectance and transmittance were taken using two different materials: Cr and Pd. For each material, three different samples were produced in the same production run, therefore the complex refractive index $N = n + ik$ is assumed to be equal for all three individual samples of a material. What can differ on the other hand is the thickness of the individual samples, as was already shown in Section 5.2, where the thickness in between samples of one material differed already just shortly after production. A correction for the incident angle of the setup was also taken into account, as the initial incident angle needed to be manually adjusted for each measurement and is expected to be in the range of $-2°$ to $2°$. For each of the six samples, three measurements were performed: reflectance, transmission with the material layer facing the laser source, and transmission with the glass layer facing the laser source. It was found that fitting multiple samples simultaneously yielded the most promising results, as the extinction coefficient is strongly correlated for reflectance and anti-correlated for transmittance with the thickness of the thin layer. However, it was not possible to obtain a valid fit result that included all samples of a kind. This will be discussed in more detail in the following subsections. The fits were conducted using the **Least Squares** method of the `minuit`-minimizer, that is based on the `Minuit2` C++ library and supported by scientists at CERN [33].

6.4.1 Transmittance: Material facing the Laser

For the case where the material faces the laser, the reflectance and transmittance of the air-**Cr**/**Pd**-glass system can be determined using Equations 3.33. The portion of light that is transmitted through the thin layer then encounters the glass-air interface, where back reflections or further transmission out of the sample can occur. To account for the internal reflections within the glass when determining the transmission from glass to air (T_{23}), one can build an infinite sum of reflectances and transmittances at both the glass-air and glass-thin layer interfaces. This approach accounts for the multiple reflections and transmissions, leading to the following expression:

$$T_{123} = T_{23} + T_{23}R_{32}R_{210} + T_{23}R_{32}^2R_{210}^2 + \dots, \tag{6.1}$$

which can again be solved using the geometric series analogously to Equation 3.29. To get the Transmittance of the full system one multiplies T_{012} and uses the relation from Equation 3.13 to get

$$T_{0123} = \frac{T_{012}T_{23}}{1 - R_{23}R_{210}}. \tag{6.2}$$

This function was then used to fit the processed measurement results as described above. At first, the results for the three Cr samples, in the following referred to as Cr1, Cr2 and Cr3, are shown in Figure 6.8 with the associated fit parameters shown in Table 6.2.

The plots shown in Figure 6.8 present the data from the three measurements together with a fit model as described in Equation 6.2. The resulting fit parameters align well

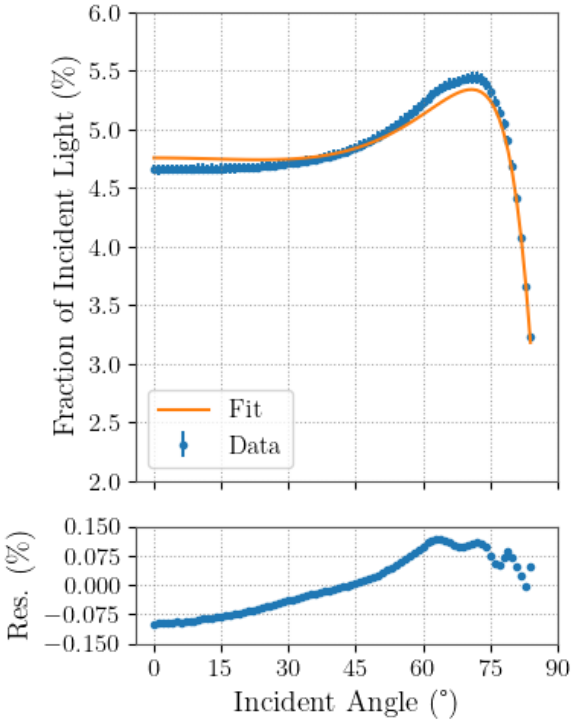

(a) Data and Fit for **Cr1**

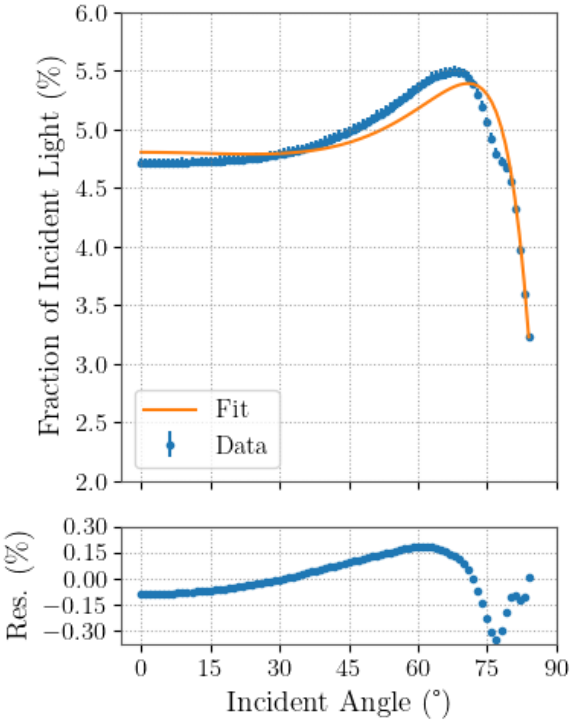

(b) Data and Fit for **Cr2**

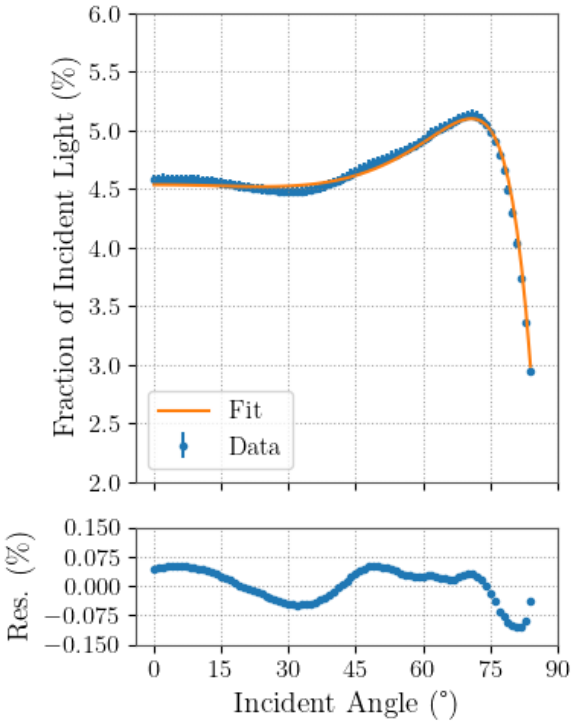

(c) Data and Fit for **Cr3**

Table 6.2: Fit parameters for the three Cr samples. Parameters without index are shared between all three sets of data.

Parameter	Value
n	2.80 ± 0.25
k	4.36 ± 0.10
d_1 (nm)	20.03 ± 0.08
d_2 (nm)	19.94 ± 0.08
d_3 (nm)	20.46 ± 0.07
θ_1 (°)	-0.64 ± 0.02
θ_2 (°)	-0.61 ± 0.02
θ_3 (°)	-0.75 ± 0.03
χ^2_{red}	4.3

Figure 6.8: Measured Transmittance of the three Cr samples with the Cr side facing the laser. The three sets of data were fitted together using a shared complex refractive index N, but with individual thicknesses for the thin layer and individual angle corrections. For the fit Equation 6.2 was used.

with the literature expectations for Cr. These were anticipated to be between the values obtained from SoN, $N_{\mathrm{Cr,SoN}} = 2.33 + 4.39i$, and the literature values, $N_{\mathrm{Cr}} = 2.69 + 4.71i$ from [24]. The target was to produce a sample thickness of 20 nm, which was measured at SoN to be approximately 19.5 nm. While the measurement of Cr3, shown in Figure 6.7c, seems to fit the theoretical model decently well, Cr1 in Figure 6.7a and Cr2 in Figure 6.7b exhibit slight divergences from the data. For Cr2, the data shows a small offset at around 76°, complicating the fit process. This reveals a general challenge: the transmittance, especially for Cr, is relatively low, at around 5%, and only increases slightly from 0° to approximately 40°. The characteristic features of this measurement are the peak at around 70° and the steep decline thereafter. These regions proved increasingly delicate to measure accurately since the laser beam begins to slightly diffract at high angles due to its non-zero radius, causing it to spread over a small elongated area instead of a single point on the sample. However, these ranges were crucial for the fit, as focusing on these regions allowed the minimizer to find local minima for the anti-correlated thickness of the layer d and the extinction coefficient k, which often behaved almost interchangeably.

Next, the results for the same type of measurement are presented for the three Pd samples, that similarly to before will be referred to as Pd1, Pd2 and Pd3. The data and the fit are shown in Figure 6.10 with the corresponding fit parameters in Table 6.3.

When comparing the results from this measurement to those of the Cr samples, some previously made observations can be further elaborated. As expected, the measurement

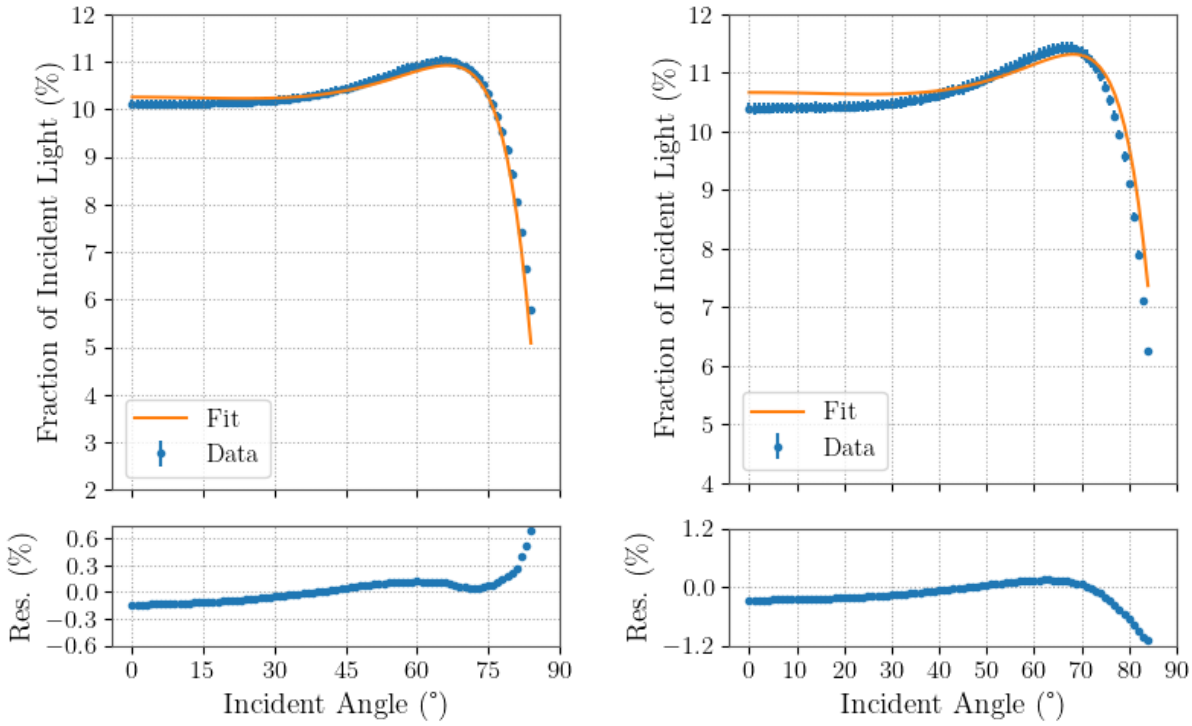

(a) Data and Fit for **Pd1**

(b) Data and Fit for **Pd2**

Figure 6.9: Measured Transmittance of the Pd samples Pd1 and Pd2 with the Pd side facing the laser. The data for each sample was fitted using the same method as before for Cr. Pd3 was also fitted together with these samples and is shown in Figure 6.10c.

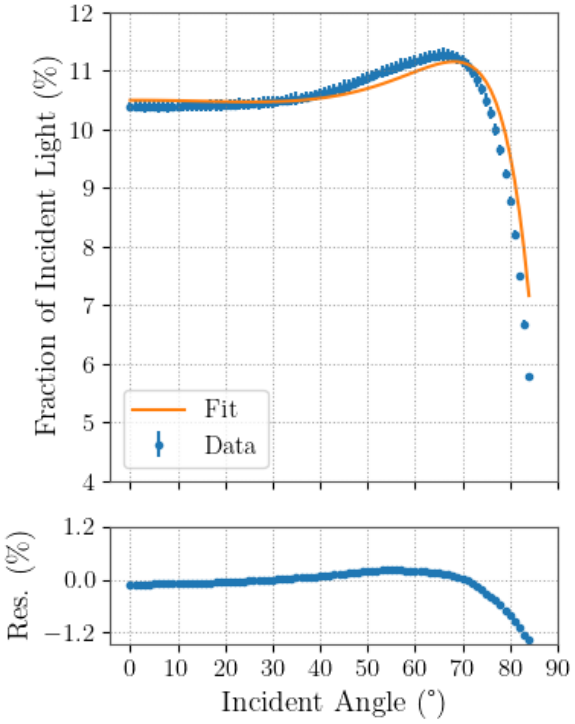

(c) Data and Fit for **Pd3**

Table 6.3: Fit parameters for the Pd samples. Parameters without index are shared between all three sets of data.

Parameter	Value
n	1.98 ± 0.09
k	4.51 ± 0.02
d_1 (nm)	14.69 ± 0.22
d_2 (nm)	14.37 ± 0.22
d_3 (nm)	14.50 ± 0.22
θ_1 (°)	-1.45 ± 0.03
θ_2 (°)	0.71 ± 0.10
θ_3 (°)	0.56 ± 0.10
χ^2_{red}	2.0

Figure 6.10: Measured Transmittance of the Pd3 sample. The sample was fitted together with Pd1 and Pd2 using a shared complex refractive index N, but with individual thicknesses for the thin layer and individual angle corrections. For the fit Equation 6.2 was used. The fit parameters are shown in Table 6.3.

results visually resemble those of the Cr samples in terms of the flat ascent for small angles and the peak at around 70°, followed by a steep descent. However, the general transmittance for Pd is roughly twice as high as for Cr, starting at around 10% and peaking at 11%. At first glance, the model seems to fit the data reasonably well, especially in the region around the peak. However, the transmittance at large angles beyond the peak could not be sufficiently matched by the model. Regarding the fit results, the previously mentioned anti-correlation clearly shows here. On the one hand, the fit converged to a real refractive index of $n = 1.98 \pm 0.09$, which is in the rough range of the literature value where $N_{\text{Pd}} = 1.61 + 3.64i$. On the other hand, the extinction coefficient k deviated further from the expected value than anticipated. This deviation appears to be accommodated by the minimizer by reducing the thickness of the samples to around 14.5 nm each, which is lower than expected. The opposing behavior of k and d, both of which are included in the phase thickness as simple factors, made the minimization of the fit very challenging with physically meaningful values. Local minima seemed to be extremely fragile in such cases. The complex refractive index given by the ellipsometer at SoN was $N_{\text{Pd,SoN}} = 1.48 + 3.44i$, which is significantly lower for both n and k, while the measurement of the thickness was significantly higher than the here fitted values and was around 22.7 nm, as would be expected by the model used here.

6.4.2 Transmittance: Glass facing the Laser

Next the other transmittance measurement shall be analyzed, where the sample was oriented with the glass side towards the laser. In this case the system of air-glass-**Cr**/**Pd**-air can be viewed as exactly the four-layer system described by Equations 3.36. The transmittance of said system is therefore entirely described by

$$T_{0123} = \frac{T_{123}(1 - R_{01})}{1 - R_{01}R_{123}}, \tag{6.3}$$

which will be used as a fit function for the following sets of data. Again, the complex refractive index is assumed constant for all the samples of one material, while the thickness is left an individual parameter for each sample. Again the results for the Cr samples are shown first, although only the measurements for samples Cr1 and Cr3 yielded data suitable for further use. For sample Cr2, a systematic error seems to have occurred, causing the intensities to drop heavily around the peak region. The data for Cr1 and Cr3 together with the fits is shown in Figure 6.11, the resulting fit parameter are presented in Table 6.4.

The fits demonstrate a similar behavior to the previous results. While the fit accurately describes the general shape of the measured data, there are systematic errors at crucial points. In Figure 6.11a, a deviation from the fit curve is observed around the peak region, similar to Figure 6.7b. Here, the measurement points drop just after the peak at

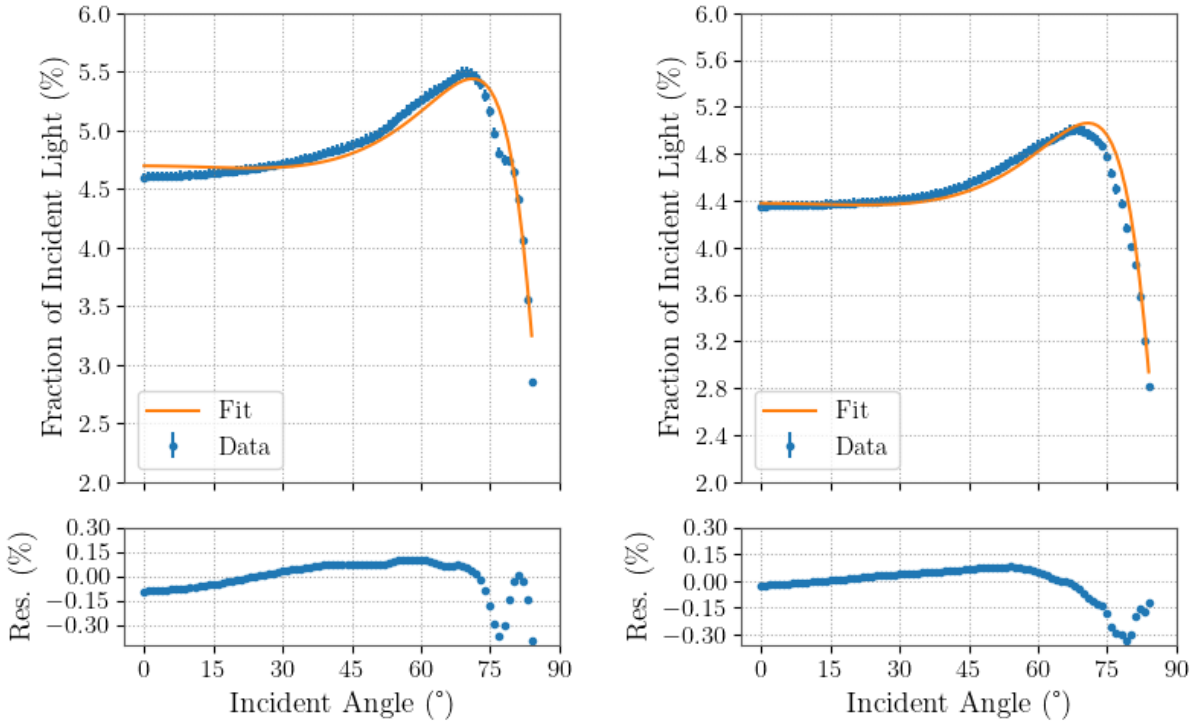

(a) Data and Fit for **Cr1**

(b) Data and Fit for **Cr3**

Figure 6.11: Data and fits for Cr1 and Cr3. As a fit model Equation 6.3 was used for both at the same time, again with shared N but individual d and θ. The fit parameters are shown in Table 6.4.

Table 6.4: Fit parameters for the three Cr samples. Parameters without index are shared between both sets of data.

Parameter	Value
n	2.83 ± 0.02
k	4.03 ± 0.01
d_1 (nm)	22.17 ± 0.08
d_3 (nm)	20.78 ± 0.16
θ_1 (°)	-1.52 ± 0.03
θ_3 (°)	-1.74 ± 0.09
χ^2_{red}	3.3

approximately 70°, before converging again with the expected course around 80°. Additionally, the fit deviates by a an absolute value of 0.1% at 0°. Figure 6.11b describes the low angles more accurately, although there is a slight structure within the residuals, which remains below 0.1% in absolute value. Once again, the range from 70° to 80° shows some discrepancies where the fit exceeds the transmittance measured by up to 0.3% at maximum. The fitted parameters fall into a similar range as the previously fitted values for these samples measured from the other side. The real refractive index n matches up within the error range, while the extinction coefficient is close but smaller by around 0.3. This, in turn, is reflected in a larger thickness estimate for d_1, while d_3 remains similar to the previous measurement.

Continuing with the results for Pd1, Pd2 and Pd3 for this measurement setup. The data sets together with the fitted model are shown in Figure 6.13 and the parameters resulting from the fit are presented in Table 6.5 for Pd1 and Pd3. These two sets of data were fitted together with the data of the transmittance measurements of the same samples and by using their fit parameters as starting values. Since the goodness of the fit, expressed by the χ^2_{red}, has subsided a little in the process for the fits from the other measurement their previously fitted results were shown before though. Also worth mentioning is, that although the same sample fitted over multiple measurements is fitted with the same thickness, the angle correction θ was an individual factor for each sample. Pd2 was later fitted in a global fit of all other measurements with Pd samples, including those shown in the next subsection. The resulting fit parameter for Pd2 are shown in Table 6.12b.
The resulting fit parameters are very close to the ones found in the previous subsections measurement setup if not concurring within the margin of error. In this case the quality of the data seems to be a bit worse off, as can be seen as dent-like structures for Pd2 and Pd3 that are not foreseen by the model as the fit visualizes by showing only small residuals with little structure from 0° to around 50°, but then losing track of the data that loses intensity for a few angles before converging again after the peak at around 80°. As for the resulting fit parameters the aforementioned from the previous measurement of Pd samples applies: the fit results form a valid minimum, even if not at the expected combination of parameters. On the other hand it was again not possible to find any stable minimum for an extinction coefficient k around the region of Pd literature values.

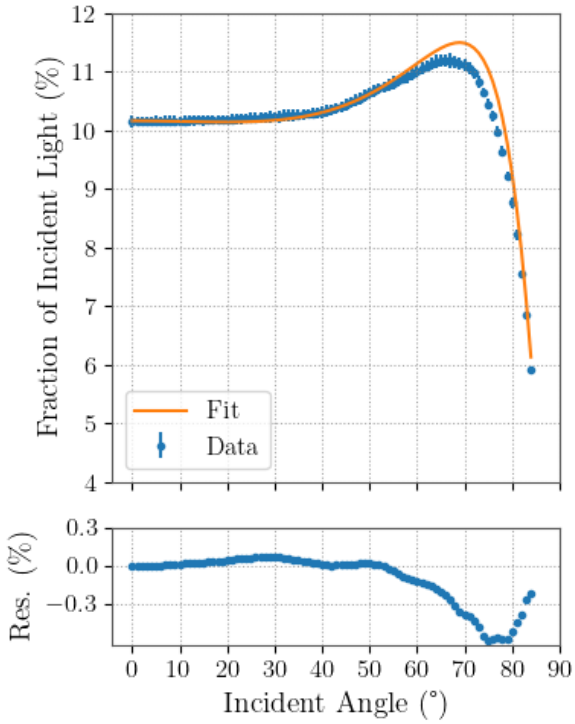

(a) Data and Fit for **Pd1**

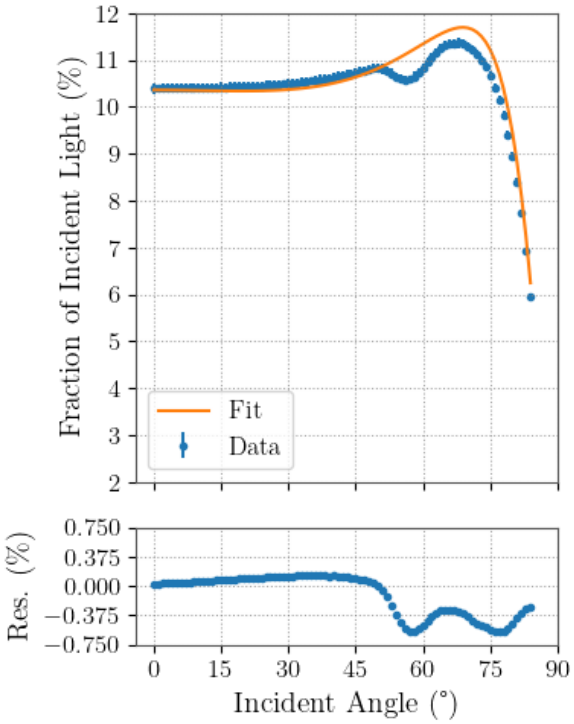

(b) Data and Fit for **Pd2**

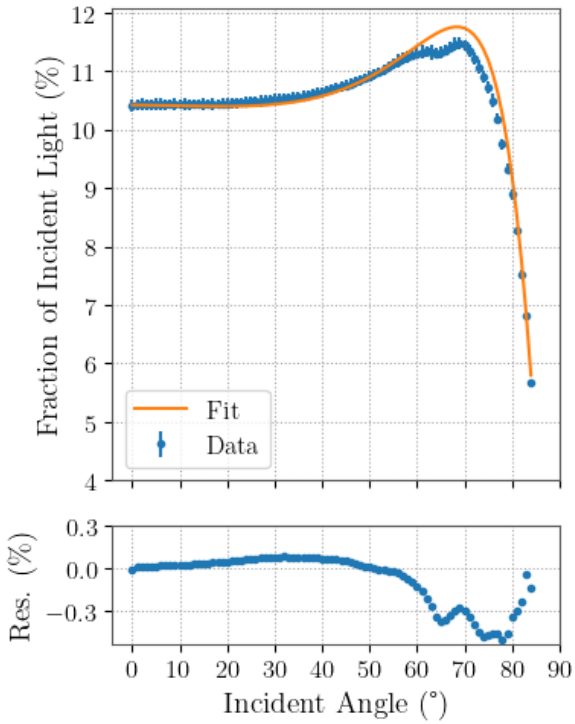

(c) Data and Fit for **Pd3**

Table 6.5: Fit parameters for Pd1 and Pd3.

Parameter	Value
n	1.96 ± 0.01
k	4.60 ± 0.02
d_2 (nm)	14.13 ± 0.09
d_3 (nm)	14.23 ± 0.09
θ_2 (°)	-1.16 ± 0.04
θ_3 (°)	-2.75 ± 0.02
χ^2_{red}	2.55

Figure 6.13: Measured Transmittance of the three Pd samples with the glass side facing the laser. For the fit Equation 6.2 was used. Table 6.5 shows the fit parameter for Pd1 and Pd3, the results for Pd2 are shown in Table 6.6

Table 6.6: Fit parameters for Pd2 resulting from a global fit over all Pd samples

Parameter	Value
n	2.00 ± 0.01
k	4.59 ± 0.02
d_2 (nm)	14.22 ± 0.08
θ_2 (°)	-2.33 ± 0.02
χ^2_{red}	3.55

6.4.3 Reflectance: Material facing the Laser

The measurements of reflectance came with the previously mentioned feature, that the measurement needed to be split in two parts due to constraints from the three legged hexapod, where one contained the small angles from 25° to 65° and the other contained large angles from 63° to 85° after which it was not possible anymore to guarantee the laser hitting the same spot on the sample anymore. The little overlap will show as places in the plot with two data points. Since switching between the two possible angle ranges is combined with a lot of physical and technical effort due to the spatial conditions in the laboratory, it was decided to first conduct all measurements for small angles for all six samples and only after switching the setup measure the larger angles. This had the side effect and possible source of error, that every sample needed to be remounted once in between small and large angles. This was not necessary for measurements of transmission, where for for the samples used here the beam path did not change while passing the sample ($\theta_0 = \theta_3$) for every angle, so the full range of angles could be measured in one run. Additionally, since the rotation table is able to rotate 360°, it was possible to carry out both directions of transmittance measurements right after each other, therefore enabling to measure at the same point from the front and back. This was only roughly achievable for the reflectance measurements.

In this case again, were the thin layer faces the laser source, a three-layer system is assumed to begin with, leading to Equation 3.33. This reflectance was extended by a term that represents the first order of photons transmit through the thin layer, but get back reflected at the following glass-air interface and then again transmitted through the thin layer. Of course there could be multiple internal reflections in between the glass-air and glass-thin layer interface, but the first additional term is already $< 0.5 \cdot 10^{-3}$ for the entire range of angles, which allows to neglect them. This results in the fit model

$$R_{0123} = R_{012} + T_{012} R_{23} T_{210}, \tag{6.4}$$

which will be used in the following data analysis for both types of samples.

Figure 6.15 shows the results from a combined fit of the three samples Cr1, Cr2 and Cr3. The fit parameters are shown in Table 6.7.

Although the fit resembles the data seemingly well around the region of the low point at about 75°, a closer look at the details is mandated here. At low angles only the measurement of the Cr3 sample shown in Figure 6.14c aligns with the data in the region below 40°

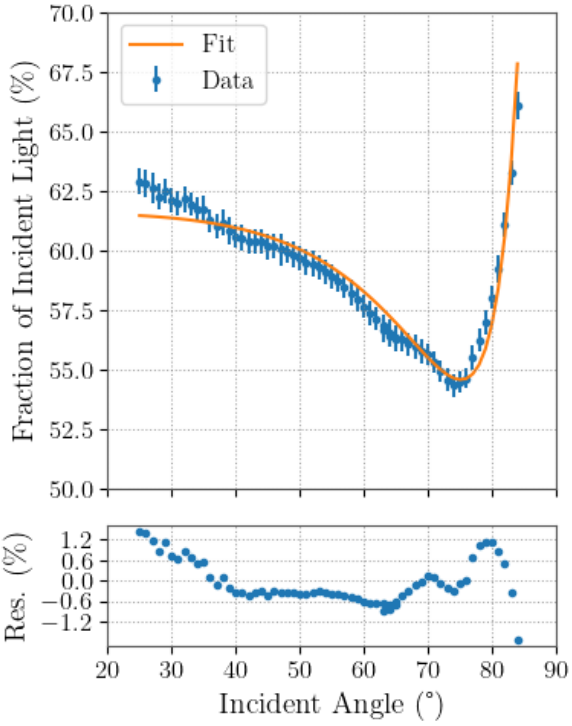

(a) Data and Fit for **Cr1**

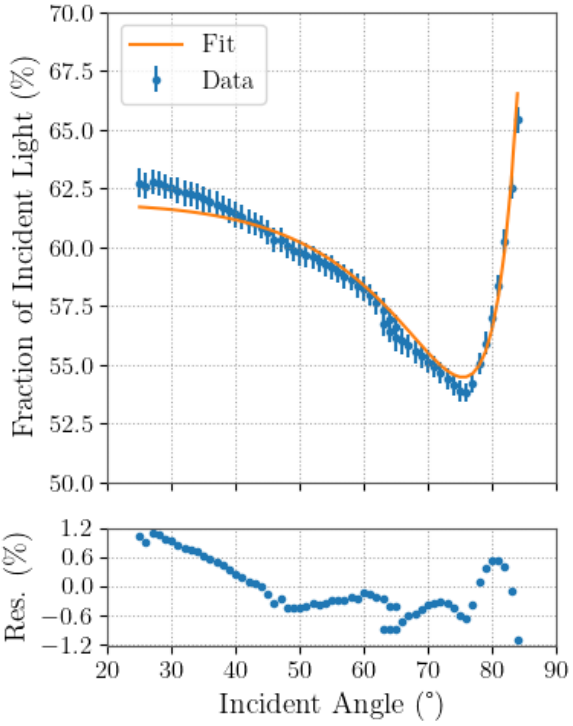

(b) Data and Fit for **Cr2**

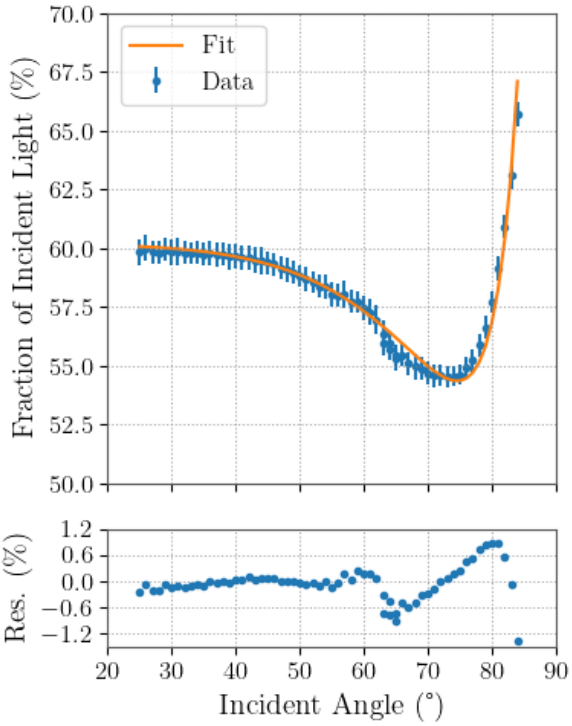

(c) Data and Fit for **Cr3**

Table 6.7: Fit parameters for the three Cr samples. Parameters without index are shared between all three sets of data.

Parameter	Value
n	3.35 ± 0.06
k	4.04 ± 0.20
d_1 (nm)	17.80 ± 2.90
d_2 (nm)	23.67 ± 1.53
d_3 (nm)	14.59 ± 1.20
θ_1 (°)	-2.14 ± 0.19
θ_2 (°)	-2.16 ± 0.29
θ_3 (°)	-1.63 ± 0.11
χ^2_{red}	1.2

Figure 6.15: Reflectance measurements of Cr1, Cr2 and Cr3 with the Cr side facing the laser. The three sets of data were fitted together using Equation 6.4 as a model with a shared complex refractive index N, but with individual thicknesses for the thin layer and individual angle corrections.

while Cr1 and Cr2 exceed the theoretical expectation, even if only in the 1%-range, which exceeds the statistical error estimations slightly. Further it is noticeable that the overlap region of small and large angles does not match up perfectly. A smoother transition could benefit the fit already in this range. The resulting fit parameters divert from the previous results especially the real refractive index n, that is shared between all three samples increased. The extinction coefficient k lies slightly below the expected value for Cr and the previous fit parameters. The thicknesses of the samples differ immensely. To understand the behavior of the fits parameters one can approximately imagine the extinction coefficient and the thickness as acting like a simple factor on the reflectance, where both a larger thickness and a larger extinction coefficient lead to a higher reflectance. The real part of the refractive index on the other hand is anti-correlated to the reflectance and at the same time shapes how sharp the drop to the minimum is, resulting in a very delicate balance which makes it hard to find potential valid minima in the fitting method.

For the last measurement results the Pd samples are shown. Here the measurement for the Pd1 sample showed an offset between small and large angles that made it impossible to justify including it in the fit. Pd2 and Pd3 are shown together with the same fit model as for the Cr samples before in Figure 6.16 with their final fit parameters presented in Table 6.8. These resulted from a combined fit of these two data sets together with data sets of the same samples for the transmission measurements using the same orientation for the sample as in this setup. As previously done, all the samples share a complex refractive index N, but also the samples of the same name share a thickness. Still every sample has an individual angular correction.

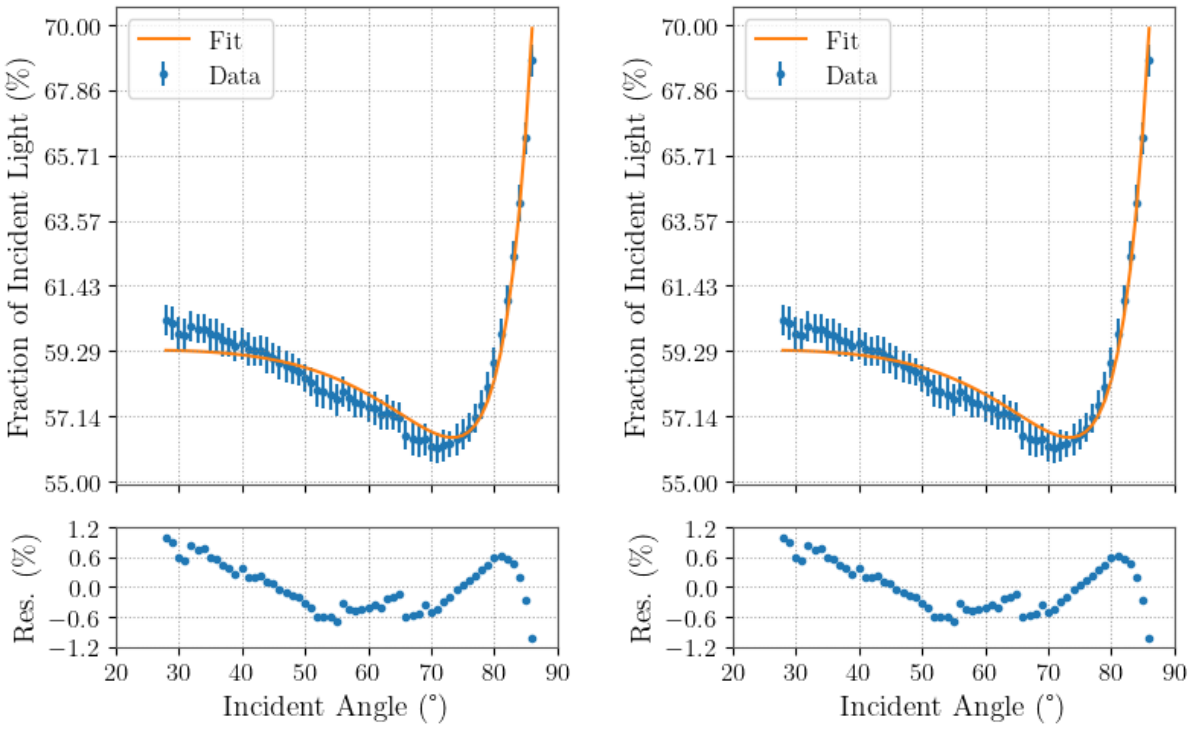

(a) Data and Fit for **Pd2**

(b) Data and Fit for **Pd3**

Figure 6.16: Data and fits for Pd2 and Pd3. As a fit model Equation 6.4 was used for both. The fit parameters are shown in Table 6.8.

Table 6.8: Fit parameters for Pd2 and Pd3 from a combined fit of both together with transmittance data from the same samples where the material faced the laser.

Parameter	Value
n	1.98 ± 0.09
k	4.51 ± 0.02
d_2 (nm)	14.37 ± 0.22
d_3 (nm)	14.50 ± 0.22
θ_2 (°)	-1.26 ± 0.05
θ_3 (°)	-1.71 ± 0.04
χ^2_{red}	2.0

The resulting fits show a similar picture than previously discussed for the Cr samples in the same setup. While the center region of the plot is decently described there are residual structures in the regions of lowest and highest angles. Here the offset in between the small angle measurement and large angle measurement is also more visible, since the large angle measurement was only started at 65° without an overlap. The resulting fit parameters have already been discussed in the previous subsection, apart from the angle offsets, that lie in an acceptable range.

6.4.4 Comparison to the Geant4 Simulation

Finally, some fit results have been reinserted into the Geant4 simulation of the sample, to demonstrate the recreation of the data using the simulation environment. The parameters used are shown in Table 6.9. The simulation was run for 10^5 events for each of the four setups. The simulation was done for two samples, Cr3 and Pd3 and from both directions for both. For the material side facing the sample, the reflectance of the sample is shown, for the glass side facing the sample the transmittance to show both models for each material. The resulting plots are shown in Figure 6.17. As can be seen, the new simulation resembles the shape of the fitted data, although there are small deviations again at very large angles, that are mostly expected from previous comparisons from the simulation to the theoretical expectations.

It was expected that the simulation matches better when the material side is facing the photon source, since these simulations aligned very well in Figure 6.6. This was very successful for the setup were the Cr3 sample faced the photon source with the material side, as can be seen in Figure 6.17a, where the simulated data matches the theoretical expectations for the properties derived from the fit for all angles. The simulation of transmittance data for Cr yielded also a to be expected result, where the simulation

Table 6.9: Fit parameters inserted into the Geant4 simulation for Cr and Pd samples.

Parameter	Cr	Pd
n	2.80	1.98
k	4.03	4.51
d_3 (nm)	20.46	14.50

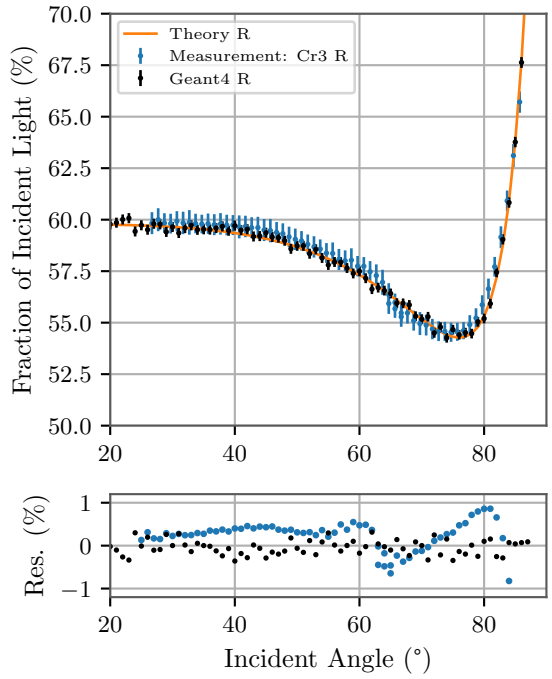

(a) Data, Fit and Simulation for **Cr3**, Reflectance

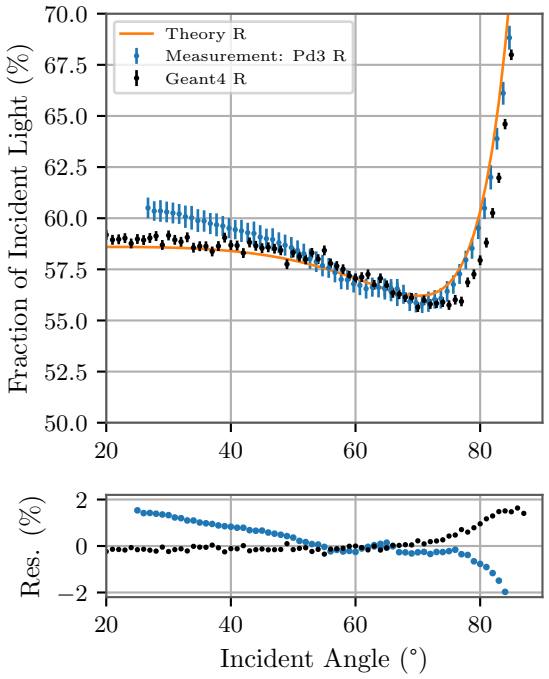

(b) Data, Fit and Simulation for **Pd3**, Reflectance

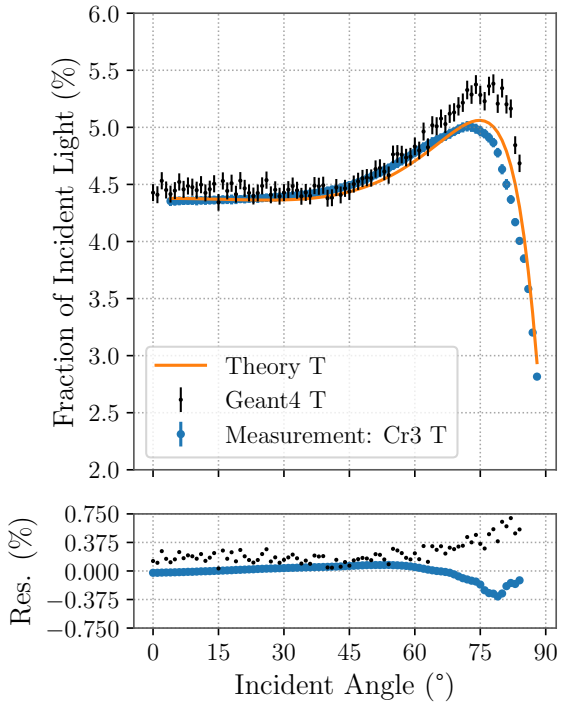

(c) Data, Fit and Simulation for **Cr3**, Transmittance - glass first

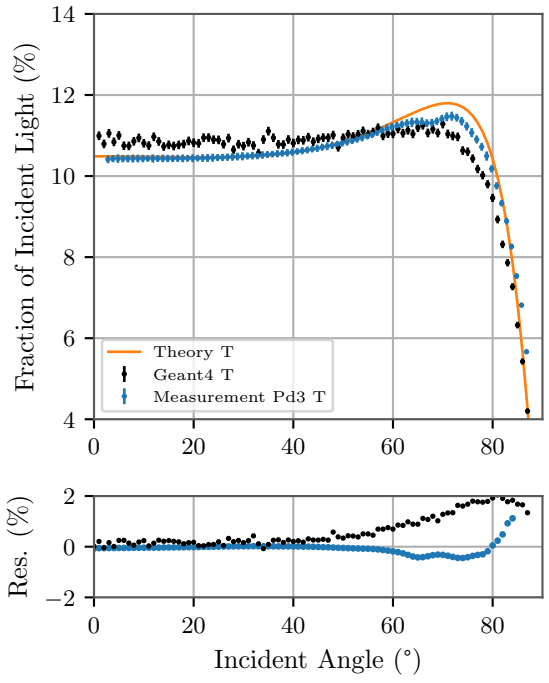

(d) Data, Fit and Simulation for **Pd3**, Transmittance - glass first

Figure 6.17: Data and fits for Cr3 and Pd3 as previously shown in Figure 6.14c, 6.16b, 6.11b and 6.12c. The fit parameters of each fit were used to create new Geant4 data that is shown in the respective plot. Underneath the residuals show the difference between each data set and the theoretical expectation.

deviates from the theoretical result around the peak region by landing a bit over half a percent higher than the expectations. It shall be noted that the errors appear large in this plot due to the nature of Poissonian statistic at comparably lower countrates. The results for the Pd results is insightful about the influence of the extinction coefficient and the thickness of the thin layer. One needs to keep in mind, that the parameters found in the minimum of the fit for the Pd samples fell below the expected thickness, but found a higher extinction coefficient than expected. This seems to cause the simulation to deviate more from the theoretical expectations for the reflectance measurement and led to a lower transmittance that theoretically expected in the peak regions, that were previously not perfectly aligned.

7 Summary and Outlook

The aim of this work was to develop a deeper understanding of optical phenomena on thin films and to further develop a model from this, which can then be implemented in a Geant4 toolkit for the simulation of PMTs used in the development of optical models for IceCube. The understanding of thin layers plays an essential part in the understanding of the detection efficiency of PMTs and therefore the entire optical model. These implementations were compared with measurements involving suitable samples with thin optical layers.

The possible behavior of electromagnetic waves reaching the glass shell of a PMT was described in great detail in Chapter 3, where the importance of a complex consideration of refractive indices and angles was derived through derivation of the reflectance and transmittance of multi-layer optical systems. This involved starting at Snell's law, that yielded complex results for angles of transmittance, which later played an important role in tracing the Fresnel coefficients at different interfaces inside a system. It was shown how these also influence the film phase thickness of an optical layer and how it affects interference effects inside a thin layer and how these affects the total reflectance and transmittance of a system resembling the shell of a PMT. Lastly it was shown how one can describe a multi layer optical structure involving a thin layer in different manifestations.

These derivations were implemented in the OMSim Geant4 framework, designed to simulate different kinds of PMTs that before this work had no special consideration of optical effects inside layers as thin as a PMTs photocathode. It was shown in Chapter 4 what changes needed to be made to the `OMSimOPBoundaryProcess` class, to mimic the effects of internal interference inside a thin layer in an environment that is not equipped to look at more than a single photon at a time and a virtual setup was created to compare the simulation to real world measurements. It was shown in Chapter 6 that the results of these implementations align with the theoretical expectations for the reflectance and transmittance of an optical system containing a thin layer from either side. While the simulations resembles the expectations very well for a setup with the photon source aimed at the thin layer, the simulation slightly deviates from these at large angles around 70° when the photons reach the glass side of the sample first. This leads to the conclusions that certain effects of these optical processes are still left to be understood all-encompassing. Especially the phenomena of imaginary angles and their effect on real physical quantities like three-dimensional trajectories or probability of reflection or transmission should be explored further. Equally desirable would be a deeper dive into the nature of film phase thickness for layers that cannot be clearly defined into a thin or non-thin layer in order to explore the behavior in these borderline cases. At this point, assumptions could be used to build a bridge between models that explicitly describe thin layers and those that are significantly thicker. Nevertheless, there is still no smooth transition between the treatment of thin and thick layers, which would be conducive to a uniform consideration of optical systems.

As a final step, these changes to the simulation of photons at thin layers were compared to six specially produced samples consisting of a 2 mm thick glass slide on which a layer as thick as 20 nm was vapor-deposited. Three samples were coated using Cr and the other three with Pd. An initial characterization was performed using commercial setups as additional possible reference. While helpful to understand optical effects and the handling of sensitive samples these results were difficult to use as the exact software methodology used remained unclear.

These samples were used in a setup equipped to perform optical measurements that were also presented in Chapter 6. For each sample a measurement of reflectance and two measurements of transmittance were performed and the results compared against the previously derived theoretical expectations. It could be shown that the theoretical expectations for the reflectance and transmittance of different optical systems can be used to describe the data recorded in the measurements decently well. Otherwise the measurements revealed many different ways for future improvement. Understanding the expected behavior of the measured quantities for different configurations of the samples' optical properties and the systems setup, it is possible the focus the measurement more strongly on characteristic parts of the angular spectrum of either reflectance or transmittance. A key starting point should be a system that ensures measurements at a constant sample thickness at all times. This involves a thoughtful preparation from production to storage and prompt measurement to not influence the thin layer physically as well as choosing a setup that takes data at characteristic points without mounting and dismounting the sample. Further, it could be promising to measure an optical system like this in a way that does not involve air as a first layer, but for example a gel or water, both of which have a refractive index closer to glass, which allows for optical phenomena like total internal refraction, that do not occur in this setup. Another interesting feature could be a construction that allows the moving arm of the first diode to be computer-controlled, so that the laser is guaranteed to reach it fully at all times. A solution to the problem that the laser cannot reliably image angles greater than 85° would also be of great value.

In summary, it can be said that research into optical phenomena on thin films has not yet been fully completed and that there is plenty of scope for further projects. In particular, the real effects of imaginary angles could make a valuable contribution to a better understanding and more precise imaging of optical systems as described here, especially due to the widespread use of PMTs in various fields of application in particle physics as well as others.

Bibliography

[1] M. G. Aartsen, et al. (IceCube Collaboration), *The IceCube Neutrino Observatory: Instrumentation and Online Systems*, JINST 12 (03) (2017) P03012, Preprint 1612.05093.

[2] L. Classen, *The mDOM - a multi-PMT digital optical module for the IceCube-Gen2 neutrino telescope*, PhD thesis, Friedrich-Alexander-Universität Erlangen-Nürnberg (2017). URL https://www.uni-muenster.de/imperia/md/content/physik_kp/agkappes/abschlussarbeiten/doktorarbeiten/1702-phd_lclassen.pdf

[3] M. Thomson, Modern Particle Physics, Cambridge University Press, Cambridge, England, 2013.

[4] A. G. Lars Bergström, Cosmology and Particle Astrophysics, Springer Berlin Heidelberg, 2004. URL http://dx.doi.org/10.1007/3-540-37719-0

[5] T. K. Gaisser, R. Engel, E. Resconi, Cosmic Rays and Particle Physics, Cambridge University Press, 2016. URL http://dx.doi.org/10.1017/CBO9781139192194

[6] U. Katz, C. Spiering, *High-energy neutrino astrophysics: Status and perspectives*, Progress in Particle and Nuclear Physics 67 (3) (2012) 651–704. URL https://www.sciencedirect.com/science/article/pii/S0146641011001189

[7] J. N. Bahcall, *Solving the mystery of the missing neutrinos*, https://www.nobelprize.org/prizes/themes/solving-the-mystery-of-the-missing-neutrinos/, [Accessed 03-08-2024] (28 April 2004).

[8] C. Grupen, Astroparticle Physics, Springer, Berlin, Germany, 2010.

[9] M. Unland, *Studies on dark rates induced by radioactive decays of the multi-PMT digital optical module for future IceCube extensions*, Master's thesis, Westfälische Wilhelms-Universität Münster (2017). URL https://www.uni-muenster.de/imperia/md/content/physik_kp/agkappes/abschlussarbeiten/masterarbeiten/1712-ma_munland.pdf

[10] R. S. Busse, *Setup and commissioning of a test stand for detailed investigations of quantum efficiency characteristics of photomultiplier tubes, and initial studies for icecube-gen2*, Master's thesis, Westfälische Wilhelms-Universität Münster (2017). URL https://www.uni-muenster.de/imperia/md/content/physik_kp/agkappes/abschlussarbeiten/masterarbeiten/1703-ma_rbusse.pdf

[11] R. e. a. Abbasi, *Icetop: The surface component of icecube*, Nuclear Instruments and Methods in Physics Research Section A: Accelerators, Spectrometers, Detectors and Associated Equipment 700 (2013) 188–220. URL http://dx.doi.org/10.1016/j.nima.2012.10.067

[12] M. Aartsen, et al., *Search for astrophysical tau neutrinos in three years of icecube data*, Physical Review D 93 (2). URL http://dx.doi.org/10.1103/PhysRevD.93.022001

[13] M. G. A. und Andere, *Icecube-gen2: the window to the extreme universe*, Journal of Physics G: Nuclear and Particle Physics 48 (6) (2021) 060501. URL https://dx.doi.org/10.1088/1361-6471/abbd48

[14] M. A. U. Elorrieta, *Development, simulation, and characterisation of a novel multi-pmt optical module for icecube upgrade with emphasis on detailed understanding of photomultiplier performance parameters*, Ph.D. thesis, Münster University (2023). URL https://www.uni-muenster.de/imperia/md/content/physik_kp/agkappes/abschlussarbeiten/doktorarbeiten/phd_thesis_unland.pdf

[15] H. P. K. E. Committee, Photomultiplier tubes - Basics and Applications, 4th Edition, Hamamatsu Photonics K.K., 2017. URL https://www.hamamatsu.com/resources/pdf/etd/PMT_handbook_v4E.pdf

[16] H. Fujiwara, Spectroscopic Ellipsometry: Principles and Applications, Wiley, 2007. URL http://dx.doi.org/10.1002/9780470060193

[17] D. Motta, S. Schönert, *Optical properties of bialkali photocathodes*, Nuclear Instruments and Methods in Physics Research Section A: Accelerators, Spectrometers, Detectors and Associated Equipment 539 (1–2) (2005) 217–235. URL http://dx.doi.org/10.1016/j.nima.2004.10.009

[18] B. Herold, *Simulation and measurement of optical background in the deep sea using a multi-PMT optical module*, PhD thesis, Friedrich-Alexander-Universität Erlangen-Nürnberg (FAU) (2017).

[19] *GitHub - icecube/OMSim: Geant4 framework for IceCube optical module studies — github.com*, https://github.com/icecube/OMSim, [Accessed 07-08-2024].

[20] J. Allison, K. A. et al., *Recent developments in geant4*, Nuclear Instruments and Methods in Physics Research Section A: Accelerators, Spectrometers, Detectors and Associated Equipment 835 (2016) 186–225. URL http://dx.doi.org/10.1016/j.nima.2016.06.125

[21] S. M. Riad, I. M. Salama, ADDENDUM 12E: THE "COMPLEX" SNELL'S LAW AND THE MYSTERY OF THE "COMPLEX" ANGLE OF REFRACTION, 1st Edition, McGraw-Hill Education, New York, 2020. URL https://www.accessengineeringlibrary.com/content/book/9781260457148/back-matter/appendix35

[22] B. Schlüter, *Setup and commissioning of an ellipsometer for the investigation of photocathodes of photomultiplier tubes*, Master's thesis, Westfälische Wilhelms-Universität Münster (2021). URL https://www.uni-muenster.de/imperia/md/content/physik_kp/agkappes/abschlussarbeiten/masterarbeiten/masterarbeit_berit_schluter.pdf

[23] e. a. Schlüter, Berit, *Detailed investigations of pmts in optical sensors for neutrino telescopes such as icecube upgrade*, in: Proceedings of 38th International Cosmic Ray Conference — PoS(ICRC2023), ICRC2023, Sissa Medialab, 2023, p. 984. URL http://dx.doi.org/10.22323/1.444.0984

[24] *Refractive index of Chromium (Cr) - Sytchkova — refractiveindex.info*, https://refractiveindex.info/?shelf=main&book=Cr&page=Sytchkova, [Accessed 01-08-2024].

[25] *Refractive index of Pd (Palladium) - Palm — refractiveindex.info*, https://refractiveindex.info/?shelf=main&book=Pd&page=Palm, [Accessed 01-08-2024].

[26] M. P. Universität Münster, *Deposition — uni-muenster.de*, https://www.uni-muenster.de/MNF/equipment/deposition.html#anchor_1_22, [Accessed 18-07-2024].

[27] *Multi Hearth Evaporators - BeamTec GmbH — beamtec.de*, https://www.beamtec.de/en/multi-hearth-evaporators/, [Accessed 18-07-2024].

[28] J. Singh, F. Quli, D. E. Wolfe, J. T. Schriempf, J. Singh, *An overview: Electron beam-physical vapor deposition technology-present and future applications*, Applied Research Laboratory, Pennsylvania State University, USA.

[29] M. P. Universität Münster, *Metrology — uni-muenster.de*, https://www.uni-muenster.de/MNF/equipment/metrology.html#anchor_1_46, [Accessed 19-07-2024].

[30] J. Woollam, *M-2000 Ellipsometer - brochure*, https://www.jawoollam.com/download/pdfs/m-2000-brochure.pdf, [Accessed 19-07-2024] (2024).

[31] M. Spengler, *Monochromator - Berthold Technologies GmbH & Co.KG*, https://www.berthold.com/de/bioanalytik/wissen/glossar-bioanalytik/monochromator/, [Accessed 05-08-2024].

[32] B. Schlüter, private communication.

[33] H. Dembinski, the iminuit team, *About - what is iminuit?*, https://scikit-hep.org/iminuit/about.html, [Accessed 07-08-2024] (2022).

Acknowledgements

First of all I want to thank the the entire group of the AG Kappes for creating an amazing environment to familiarize myself with a highly specialized topic and for always being on hand with help, advice and good spirit when you get stuck. It was always fun coming to the office.

Special thanks to Prof. Alexander Kappes for making this possible and for always being an attentive, helpful and approachable leader. Secondly I want to thank Apl. Prof. Alfons Khoukaz for being my second examiner and for always giving constructive feedback, not least during two previous oral exams. University is dependent on great teachers that also excel as executives and I want again thank both of you for achieving this in the Institute of Nuclear Physics.

I want to thank Berit Schlüter for being a super fun and extremely capable supervisor who always had a creative idea how to solve a new problem and Martin Unland, who helped me no less by patiently introducing me to a great range of topics from programming do's and don'ts to in-depth physical derivations. I learned so much from both of you and I could not be more grateful. I could keep thanking every single person in the group for so many things... You are all amazing, I could not have hoped for a better group.

Ich danke unendlich meiner Mutter Carmen für ihre ermutigenden Worte und die Kaffeauszeit am Dienstag, sowie meiner Oma Pilar, dass sie mein Gebrabbel am geduldigsten von allen ertragen hat und immer für eine Umarmung erreichbar war. Außerdem hat sie heute Geburtstag, also: ¡Feliz cumpleaños!

Und zuletzt möchte ich mir selber danken. Dafür, dass ich optimistisch geblieben bin und bis zuletzt an mich geglaubt habe auch wenn der Weg steinig war. Und dafür, dass ich viel gelernt habe und mein Ziel erreichen konnte.